

Early Growth in a Perturbed Universe: Dark Matter Halo Properties in 2LPT and ZA  
Simulations

By

Daniel J. Sissom

Dissertation

Submitted to the Faculty of the  
Graduate School of Vanderbilt University  
in partial fulfillment of the requirements  
for the degree of

DOCTOR OF PHILOSOPHY

in

PHYSICS

August, 2014

Nashville, TN

Approved:

Date:

---

Jocelyn K. Holley-Bockelmann, Ph.D.

---

Andreas A. Berlind, Ph.D.

---

David A. Weintraub, Ph.D.

---

Shane M. Hutson, Ph.D.

---

Robert J. Scherrer, Ph.D.

## **ACKNOWLEDGMENTS**

This is where you thank the people that made your work possible: grant awarding agencies, advisers, your committee, mom and dad, whatever.

# TABLE OF CONTENTS

	Page
<b>ACKNOWLEDGMENTS</b> . . . . .	<b>i</b>
<b>LIST OF TABLES</b> . . . . .	<b>vi</b>
<b>LIST OF FIGURES</b> . . . . .	<b>vii</b>
<b>I Introduction</b> . . . . .	<b>1</b>
I.1 The Early Universe . . . . .	1
I.1.1 The CMB Epoch . . . . .	1
I.1.1.1 Recombination . . . . .	1
I.1.1.2 The Cosmic Microwave Background . . . . .	2
I.1.1.3 Wilkinson Microwave Anisotropy Probe . . . . .	2
I.1.1.4 Baryon Acoustic Oscillations . . . . .	2
I.1.2 Dark Matter Halo Formation . . . . .	2
I.1.2.1 Collapse . . . . .	2
I.1.2.2 Accretion . . . . .	2
I.1.2.3 Mergers . . . . .	2
I.1.2.4 Large-scale Structure . . . . .	2
I.1.3 Halo Properties . . . . .	2
I.1.3.1 Measurements . . . . .	2
I.1.3.2 Mass . . . . .	3
I.1.3.3 Density . . . . .	3
I.1.3.4 Concentration . . . . .	3
I.1.3.5 Spin . . . . .	3
I.1.3.6 Environment . . . . .	3
I.1.4 Baryonic Processes . . . . .	3
I.1.4.1 Gas . . . . .	3
I.1.4.2 The First Stars . . . . .	3
I.1.4.3 Supernovae . . . . .	3
I.1.4.4 The Intergalactic Medium . . . . .	3
I.1.4.5 Supermassive Black Holes . . . . .	4
I.1.4.6 Active Galactic Nuclei . . . . .	4
I.1.4.7 Reionization . . . . .	4
I.2 Computational Theory . . . . .	4
I.2.1 Simulation Initialization . . . . .	4
I.2.1.1 Initial Conditions and the Surface of Last Scattering . . . . .	4
I.2.1.2 The Zel'dovich Approximation . . . . .	4

	I.2.1.3	Second-order Lagrangian Perturbation Theory . . . . .	4
I.2.2		N-body Simulations . . . . .	4
	I.2.2.1	Early Simulations . . . . .	4
	I.2.2.2	Gravity . . . . .	5
	I.2.2.3	Orbit Integration . . . . .	5
	I.2.2.4	Tree Algorithms . . . . .	5
	I.2.2.5	Mesh Algorithms . . . . .	5
I.2.3		Dark Matter Halos in N-body Simulations . . . . .	5
	I.2.3.1	Spherical Overdensity . . . . .	5
	I.2.3.2	Friends-of-Friends . . . . .	5
<b>II</b>		<b>Numerical Methods . . . . .</b>	<b>6</b>
II.1		The ACCRE Compute Cluster . . . . .	6
	II.1.1	Compute Nodes . . . . .	6
		II.1.1.1 x86_64 Nodes . . . . .	6
		II.1.1.2 GPU Nodes . . . . .	6
	II.1.2	Network . . . . .	6
	II.1.3	Filesystem . . . . .	6
	II.1.4	Scheduling . . . . .	6
II.2		Initialization Code . . . . .	6
	II.2.1	Sampling the Power Spectrum . . . . .	7
		II.2.1.1 Cosmological Parameters . . . . .	7
		II.2.1.2 Sampling . . . . .	7
	II.2.2	Particle Displacement with ZA . . . . .	7
	II.2.3	Particle Displacement with 2LPT . . . . .	7
II.3		Simulations with GADGET-2 . . . . .	7
	II.3.1	Fundamentals of GADGET . . . . .	7
		II.3.1.1 Force Calculation and Softening . . . . .	7
		II.3.1.2 Trees . . . . .	7
		II.3.1.3 Parallelization . . . . .	8
		II.3.1.4 Metrics . . . . .	8
	II.3.2	Enhancements with GADGET-2 . . . . .	8
	II.3.3	Simulations . . . . .	8
II.4		Halo Finding with ROCKSTAR . . . . .	9
	II.4.1	Halo Identification . . . . .	9
		II.4.1.1 Subsubsection1 . . . . .	9
		II.4.1.2 Subsubsection2 . . . . .	9
	II.4.2	Subsection2 . . . . .	9
	II.4.3	Halo Catalogs . . . . .	10
II.5		CROSSMATCH . . . . .	10
	II.5.1	Subsection1 . . . . .	10
		II.5.1.1 Subsubsection1 . . . . .	10
		II.5.1.2 Subsubsection2 . . . . .	10
	II.5.2	Subsection2 . . . . .	11

II.6	Analysis and Plotting . . . . .	11
II.6.1	Python and Packages Used . . . . .	11
II.6.1.1	NumPy . . . . .	11
II.6.1.2	Matplotlib . . . . .	11
II.6.1.3	SciPy . . . . .	12
II.6.1.4	StatsModels . . . . .	12
II.6.2	Non-linear Least Squares Fitting . . . . .	12
II.6.2.1	CurveFit . . . . .	12
II.6.2.2	Model Functions . . . . .	12
II.6.2.3	Initial Guess . . . . .	12
II.6.2.4	Fit Coefficients . . . . .	12
II.6.3	Halo Properties and the BGC2 Format . . . . .	12
II.6.3.1	Rockstar Output and Post-processing . . . . .	12
II.6.3.2	The BGC2 Binary File Format . . . . .	12
II.6.3.3	Spherical Overdensity Halo Particles . . . . .	13
II.6.4	Density Profiles . . . . .	13
II.6.4.1	Binning . . . . .	13
II.6.4.2	Fitting . . . . .	13
II.6.4.3	Mass Profiles . . . . .	13
II.6.4.4	Characterization of Uncertainty . . . . .	13
II.6.4.5	Halo Properties . . . . .	13
II.6.5	Cross-matched Halo Catalogue . . . . .	13
II.6.5.1	Aggregation . . . . .	13
II.6.5.2	Filtering . . . . .	13
II.6.6	Halo Comparison . . . . .	14
II.6.6.1	Match Verification . . . . .	14
II.6.6.2	Morphology . . . . .	14
II.6.6.3	Density Profiles . . . . .	14
II.6.7	Difference Histograms . . . . .	14
II.6.7.1	Binning . . . . .	14
II.6.7.2	Fitting . . . . .	14
II.6.7.3	Mass Quartiles . . . . .	14
II.6.8	Redshift Trends . . . . .	14
II.6.8.1	Mean and Standard Deviation . . . . .	14
II.6.8.2	Skew . . . . .	15
II.6.8.3	Kurtosis . . . . .	15
II.6.9	2-D Histograms . . . . .	17
II.6.9.1	Binning and Plotting . . . . .	17
II.6.9.2	Fitting . . . . .	17
II.7	Automation . . . . .	17
II.7.1	Subsection . . . . .	17
II.7.1.1	Subsubsection . . . . .	17
II.7.1.2	Subsubsection . . . . .	17
II.7.2	Subsection . . . . .	17

<b>III</b>	<b>Exploring Dark Matter Halo Populations in 2LPT and ZA Simulations . . .</b>	<b>18</b>
III.1	Introduction . . . . .	18
III.2	Numerical Methods . . . . .	23
III.3	Results . . . . .	27
III.3.1	Individual halo pairs . . . . .	28
III.3.2	Difference distributions of halo properties . . . . .	28
III.3.3	Trends with redshift . . . . .	29
III.3.4	Trends with halo mass . . . . .	32
III.3.5	Alternate fractional difference distributions . . . . .	33
III.4	Discussion . . . . .	34
III.5	Conclusion . . . . .	36
<b>IV</b>	<b>Supermassive Black Holes and Their Hosts . . . . .</b>	<b>43</b>
IV.1	Introduction . . . . .	43
IV.1.1	Galaxy Properties . . . . .	43
IV.1.1.1	Color . . . . .	43
IV.1.1.2	Morphology . . . . .	44
IV.1.2	Supermassive Black Hole Properties . . . . .	45
IV.1.3	Correlations . . . . .	48
IV.1.3.1	The M-Sigma Relation . . . . .	48
IV.1.3.2	The Fundamental Plane . . . . .	50
IV.1.3.3	The Green Valley . . . . .	51
IV.2	Galaxy Evolution . . . . .	53
IV.2.1	Dark Matter Halos . . . . .	53
IV.2.2	Galaxy Mergers . . . . .	54
IV.3	Supermassive Black Hole Growth . . . . .	55
IV.3.1	Binary Mergers . . . . .	55
IV.3.1.1	Dynamical Friction and Inspiral . . . . .	55
IV.3.1.2	The Final Parsec Problem . . . . .	56
IV.3.1.3	Gravitational Waves and Recoil Kicks . . . . .	56
IV.3.2	Accretion . . . . .	60
IV.3.2.1	Bondi-Hoyle-Lyttleton Accretion . . . . .	60
IV.3.2.2	Disk Accretion and Active Galactic Nuclei . . . . .	62
IV.4	Conclusion . . . . .	63
IV.4.1	Correlations . . . . .	63
IV.4.2	Open Questions . . . . .	63
<b>V</b>	<b>Conclusion . . . . .</b>	<b>65</b>
	<b>BIBLIOGRAPHY . . . . .</b>	<b>66</b>

## LIST OF TABLES

Table	Page
III.1	Coefficients for linear least squares fits from Figure III.3. . . . . 30

## LIST OF FIGURES

Figure	Page
II.1 Potential and force softening. . . . .	8
II.2 Barnes-Hut oct-tree in two dimensions. . . . .	8
II.3 Domain decomposition. . . . .	9
II.4 Force parallelism. . . . .	10
II.5 Energy conservation for an initially isothermal gas sphere. . . . .	11
III.1 Comparison of matched 2LPT and ZA halos . . . . .	38
III.2 Histograms of $\Delta M_{\text{vir}}$ and $\Delta c$ . . . . .	39
III.3 Statistics as functions of redshift for generalized normal fits . . . . .	40
III.4 $\Delta M_{\text{vir}}$ and $\Delta c$ as a function of $M_{\text{vir,avg}}$ . . . . .	41
III.5 Fractional error distribution statistics as functions of redshift . . . . .	42
IV.1 The Hubble tuning fork . . . . .	45
IV.2 Maser orbits fit to a warped disk for NGC4258 . . . . .	47
IV.3 The M- $\sigma$ relation for galaxies with dynamical measurements . . . . .	49
IV.4 The fundamental plane for elliptical galaxies . . . . .	51
IV.5 Distribution of the fraction of galaxies containing AGN . . . . .	52
IV.6 Rotation curves for 21 Sc galaxies . . . . .	53
IV.7 Gravitational waveform for a black hole binary merger . . . . .	58
IV.8 Gravitational wave recoil velocity from black hole mergers . . . . .	60



# **CHAPTER I**

## **Introduction**

Text goes here. This is where we'll talk about the purpose of the project and the layout of this document.

The structure of this document is as follows: The remainder of this chapter, Chapter I, provides an introduction to the early universe and the processes that lead to galaxy-hosting dark matter halos, as well as the fundamentals of the computational theory for the numerical methods relevant to this discussion. Chapter II examines in more detail the specific numerical methods used for this work, with emphasis on the methodologies of the codes themselves, how they are implemented in the context of the overall simulation and analysis pipeline, and the results obtained at each step. Chapter III is a direct representation of the published paper which (more succinctly) presents an overview of the numerical methods and the main results in this work. Chapter IV is primarily the same material as previously submitted to fulfill the requirements of the Qualifying Exam, and is slightly edited to better suit the tone of this document. Chapter V concludes with a discussion of the results in this work and the greater implications to the overall field.

### **I.1 The Early Universe**

Text goes here.

#### **I.1.1 The CMB Epoch**

Text goes here.

##### **I.1.1.1 Recombination**

Text goes here.

### **I.1.1.2 The Cosmic Microwave Background**

Text goes here.

### **I.1.1.3 Wilkinson Microwave Anisotropy Probe**

Text goes here.

### **I.1.1.4 Baryon Acoustic Oscillations**

Text goes here.

## **I.1.2 Dark Matter Halo Formation**

Text goes here.

### **I.1.2.1 Collapse**

Text goes here.

### **I.1.2.2 Accretion**

Text goes here.

### **I.1.2.3 Mergers**

Text goes here.

### **I.1.2.4 Large-scale Structure**

Text goes here.

## **I.1.3 Halo Properties**

Text goes here.

### **I.1.3.1 Measurements**

Text goes here.

### **I.1.3.2 Mass**

Text goes here.

### **I.1.3.3 Density**

Text goes here.

### **I.1.3.4 Concentration**

Text goes here.

### **I.1.3.5 Spin**

Text goes here.

### **I.1.3.6 Environment**

Text goes here.

## **I.1.4 Baryonic Processes**

Text goes here.

### **I.1.4.1 Gas**

Text goes here.

### **I.1.4.2 The First Stars**

Text goes here.

### **I.1.4.3 Supernovae**

Text goes here.

### **I.1.4.4 The Intergalactic Medium**

Text goes here.

#### **I.1.4.5 Supermassive Black Holes**

Text goes here.

#### **I.1.4.6 Active Galactic Nuclei**

Text goes here.

#### **I.1.4.7 Reionization**

Text goes here.

### **I.2 Computational Theory**

Text goes here.

#### **I.2.1 Simulation Initialization**

Text goes here.

##### **I.2.1.1 Initial Conditions and the Surface of Last Scattering**

Text goes here.

##### **I.2.1.2 The Zel'dovich Approximation**

Text goes here.

##### **I.2.1.3 Second-order Lagrangian Perturbation Theory**

Text goes here.

#### **I.2.2 N-body Simulations**

Text goes here.

##### **I.2.2.1 Early Simulations**

Text goes here.

#### **I.2.2.2 Gravity**

Text goes here.

#### **I.2.2.3 Orbit Integration**

Text goes here.

#### **I.2.2.4 Tree Algorithms**

Text goes here.

#### **I.2.2.5 Mesh Algorithms**

Text goes here.

### **I.2.3 Dark Matter Halos in N-body Simulations**

Text goes here.

#### **I.2.3.1 Spherical Overdensity**

Text goes here.

#### **I.2.3.2 Friends-of-Friends**

Text goes here.

## **CHAPTER II**

### **Numerical Methods**

Text goes here. Here, we will discuss the computational tools used, their inner workings, and how they are implemented to accomplish their purpose in the pipeline.

#### **II.1 The ACCRE Compute Cluster**

Text goes here.

##### **II.1.1 Compute Nodes**

Text goes here.

###### **II.1.1.1 x86\_64 Nodes**

Text goes here.

###### **II.1.1.2 GPU Nodes**

Text goes here.

##### **II.1.2 Network**

Text goes here.

##### **II.1.3 Filesystem**

Text goes here.

##### **II.1.4 Scheduling**

Text goes here.

#### **II.2 Initialization Code**

Text goes here.

## **II.2.1 Sampling the Power Spectrum**

Text goes here.

### **II.2.1.1 Cosmological Parameters**

Text goes here.

### **II.2.1.2 Sampling**

Text goes here.

## **II.2.2 Particle Displacement with ZA**

Text goes here.

## **II.2.3 Particle Displacement with 2LPT**

Text goes here.

## **II.3 Simulations with GADGET-2**

We use the massively parallel TreeSPH cosmological N-body simulation code GADGET-2 for the dark matter simulations presented in this work. In this section, we begin with a discussion of the fundamental concepts presented in the original GADGET code, then proceed to the improvements made in the GADGET-2 code.

### **II.3.1 Fundamentals of GADGET**

Text goes here.

#### **II.3.1.1 Force Calculation and Softening**

Text goes here.

#### **II.3.1.2 Trees**

Text goes here.

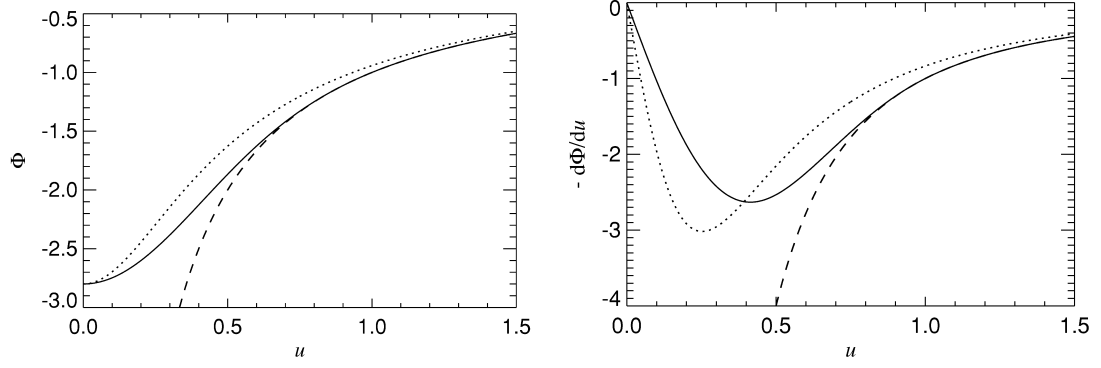


Figure II.1: Potential (*left*) and force (*right*) softening.

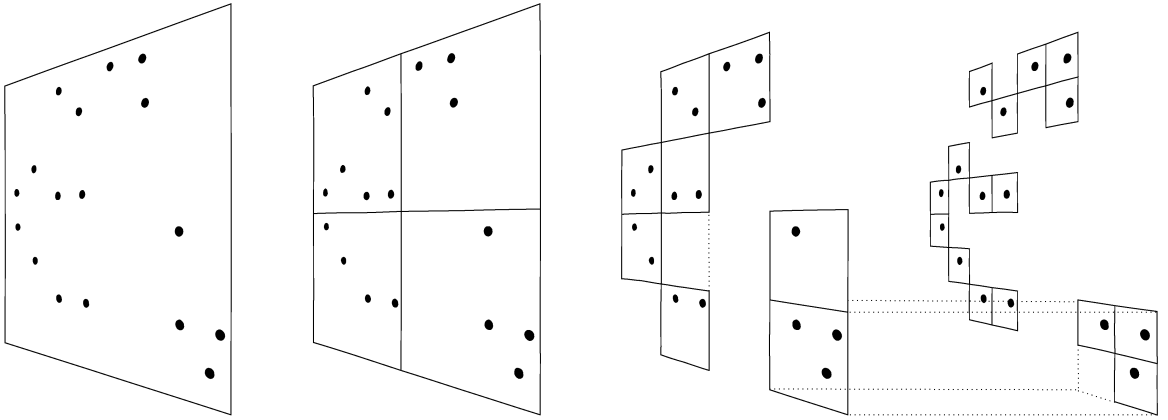


Figure II.2: Barnes-Hut oct-tree in two dimensions.

### II.3.1.3 Parallelization

Text goes here.

### II.3.1.4 Metrics

Text goes here.

## II.3.2 Enhancements with GADGET-2

Text goes here.

## II.3.3 Simulations

Text goes here.



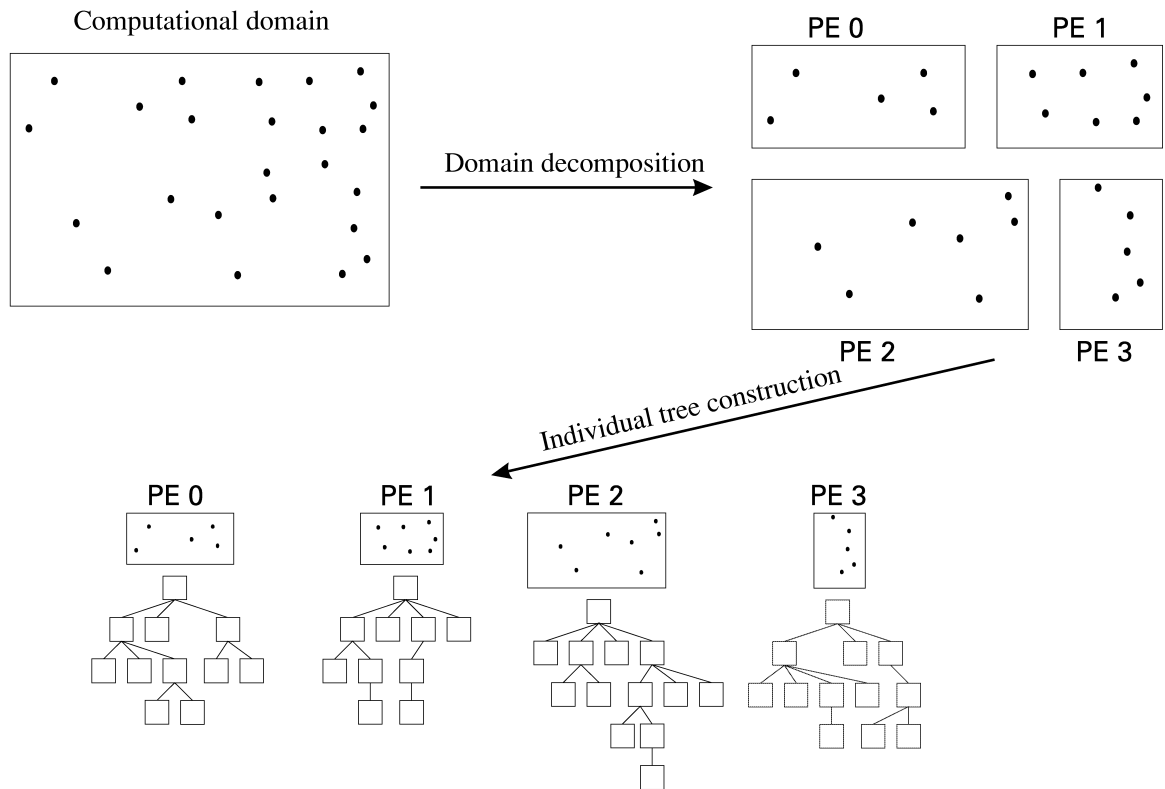


Figure II.3: Domain decomposition.

## II.4 Halo Finding with ROCKSTAR

Text goes here.

### II.4.1 Halo Identification

Text goes here.

#### II.4.1.1 Subsubsection1

Text goes here.

#### II.4.1.2 Subsubsection2

Text goes here.

### II.4.2 Subsection2

Text goes here.

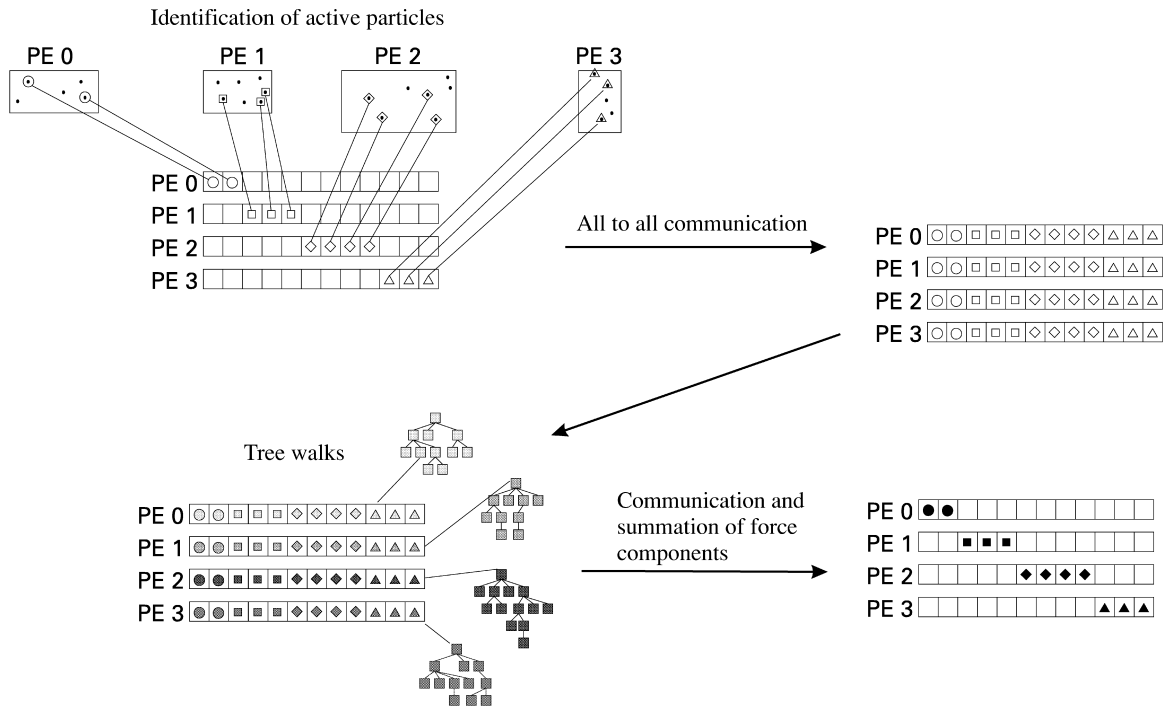


Figure II.4: Force parallelism.

### II.4.3 Halo Catalogs

Text goes here.

## II.5 CROSSMATCH

Text goes here.

### II.5.1 Subsection1

Text goes here.

#### II.5.1.1 Subsubsection1

Text goes here.

#### II.5.1.2 Subsubsection2

Text goes here.

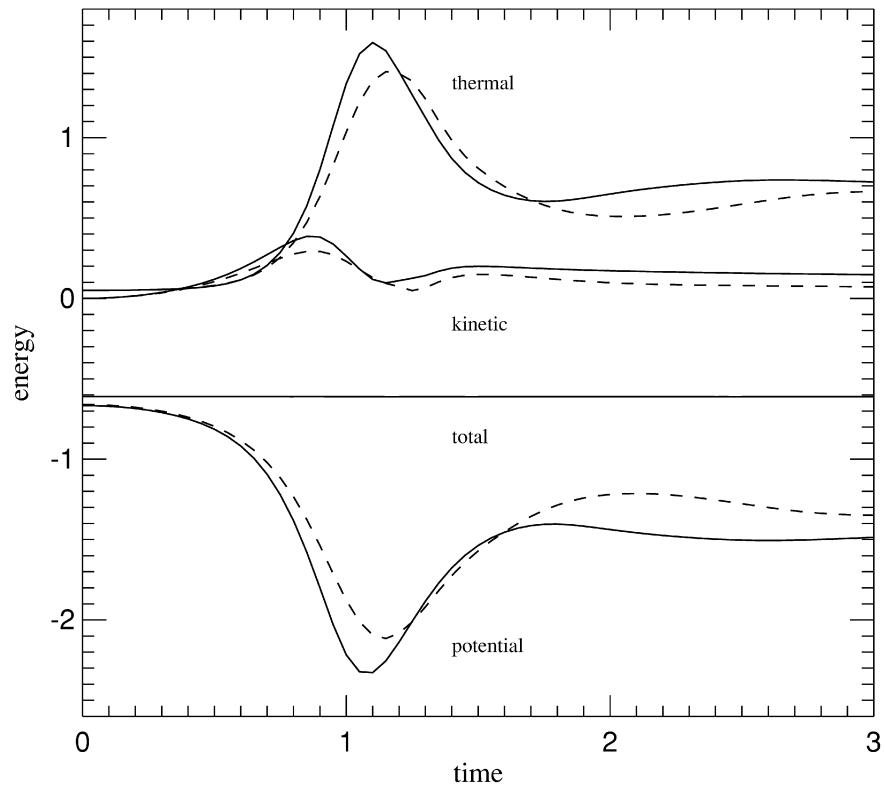


Figure II.5: Energy conservation for an initially isothermal gas sphere.

## II.5.2 Subsection2

Text goes here.

## II.6 Analysis and Plotting

Text goes here.

### II.6.1 Python and Packages Used

Text goes here.

#### II.6.1.1 NumPy

Text goes here.

#### II.6.1.2 Matplotlib

Text goes here.

### **II.6.1.3 SciPy**

Text goes here.

### **II.6.1.4 StatsModels**

Text goes here.

## **II.6.2 Non-linear Least Squares Fitting**

Text goes here.

### **II.6.2.1 CurveFit**

Text goes here.

### **II.6.2.2 Model Functions**

Text goes here.

### **II.6.2.3 Initial Guess**

Text goes here.

### **II.6.2.4 Fit Coefficients**

Text goes here.

## **II.6.3 Halo Properties and the BGC2 Format**

Text goes here.

### **II.6.3.1 Rockstar Output and Post-processing**

Text goes here.

### **II.6.3.2 The BGC2 Binary File Format**

Text goes here.

### **II.6.3.3 Spherical Overdensity Halo Particles**

Text goes here.

## **II.6.4 Density Profiles**

Text goes here.

### **II.6.4.1 Binning**

Text goes here.

### **II.6.4.2 Fitting**

Text goes here.

### **II.6.4.3 Mass Profiles**

Text goes here.

### **II.6.4.4 Characterization of Uncertainty**

Text goes here.

### **II.6.4.5 Halo Properties**

Text goes here.

## **II.6.5 Cross-matched Halo Catalogue**

Text goes here.

### **II.6.5.1 Aggregation**

Text goes here.

### **II.6.5.2 Filtering**

Text goes here.

## **II.6.6 Halo Comparison**

Text goes here.

### **II.6.6.1 Match Verification**

Text goes here.

### **II.6.6.2 Morphology**

Text goes here.

### **II.6.6.3 Density Profiles**

Text goes here.

## **II.6.7 Difference Histograms**

Text goes here.

### **II.6.7.1 Binning**

Text goes here.

### **II.6.7.2 Fitting**

Text goes here.

### **II.6.7.3 Mass Quartiles**

Text goes here.

## **II.6.8 Redshift Trends**

Text goes here.

### **II.6.8.1 Mean and Standard Deviation**

Text goes here.

### II.6.8.2 Skew

Text goes here.

### II.6.8.3 Kurtosis

Text goes here.

The standard deviation of a function  $f(x_1, x_2, \dots, x_n)$  is, in general, given by

$$s_f = \sqrt{\sum_x \left( \frac{\partial f}{\partial x} \right)^2 s_x^2} \quad (\text{II.1})$$

with summation over all independent variables  $x$ . The generalized normal distribution

$$f(x) = \frac{\beta}{2\alpha\Gamma(1/\beta)} e^{-(|x-\mu|/\alpha)^\beta} \quad (\text{II.2})$$

with mean  $\mu$ , scale parameter  $\alpha$ , and shape parameter  $\beta$ , has excess kurtosis

$$\gamma_2 = \frac{\Gamma(5/\beta)\Gamma(1/\beta)}{\Gamma(3/\beta)^2} - 3. \quad (\text{II.3})$$

The gamma function

$$\Gamma(x) = \int_0^\infty t^{x-1} e^{-t} dt \quad (\text{II.4})$$

has the first derivative

$$\Gamma'(x) = \Gamma(x)\psi_0(x) \quad (\text{II.5})$$

where the digamma function  $\psi_0$  is the derivative of the logarithm of the gamma function and is given by

$$\psi_0(x) = \int_0^\infty \left( \frac{e^{-t}}{t} - \frac{e^{-xt}}{1-e^{-t}} \right) dt \quad (\text{II.6})$$

if the real part of  $x$  is positive.

We now apply (II.1) to (III.13) to find the standard deviation of the excess kurtosis:

$$s_{\gamma_2} = \sqrt{\left(\frac{d\gamma_2}{d\beta}\right)^2 s_\beta^2} \quad (\text{II.7})$$

$$= s_\beta \frac{d\gamma_2}{d\beta} \quad (\text{II.8})$$

$$= s_\beta \frac{d}{d\beta} \left[ \frac{\Gamma(5/\beta)\Gamma(1/\beta)}{\Gamma(3/\beta)^2} - 3 \right]. \quad (\text{II.9})$$

Making the substitution  $x = 1/\beta$  and  $dx = -1/\beta^2 d\beta$ , taking the derivative, and doing a bit of algebra, we have:

$$s_{\gamma_2} = s_\beta \frac{d\gamma_2}{dx} \frac{dx}{d\beta} \quad (\text{II.10})$$

$$= s_\beta \left( -\frac{1}{\beta^2} \right) \frac{d}{dx} \left[ \frac{\Gamma(5x)\Gamma(x)}{\Gamma(3x)} - 3 \right] \quad (\text{II.11})$$

$$= -s_\beta x^2 \left\{ \frac{\Gamma(3x)^2 \frac{d}{dx} [\Gamma(5x)\Gamma(x)] - \Gamma(5x)\Gamma(x) \frac{d}{dx} [\Gamma(3x)^2]}{\Gamma(3x)^4} \right\} \quad (\text{II.12})$$

$$= -s_\beta \frac{x^2}{\Gamma(3x)^4} \{ \Gamma(3x)^2 [5\Gamma(5x)\psi_0(5x)\Gamma(x) + \Gamma(5x)\Gamma(x)\psi_0(x)] - \Gamma(5x)\Gamma(x) [6\Gamma(3x)^2\psi_0(3x)] \} \quad (\text{II.13})$$

$$= s_\beta \frac{x^2}{\Gamma(3x)^4} \{ 6\Gamma(5x)\Gamma(3x)^2\Gamma(x)\psi_0(3x) - \Gamma(5x)\Gamma(3x)^2\Gamma(x) [5\psi_0(5x) + \psi_0(x)] \} \quad (\text{II.14})$$

$$= s_\beta \frac{x^2}{\Gamma(3x)^4} \{ \Gamma(5x)\Gamma(3x)^2\Gamma(x) [6\psi_0(3x) - 5\psi_0(5x) - \psi_0(x)] \} \quad (\text{II.15})$$

$$= s_\beta x^2 \frac{\Gamma(5x)\Gamma(x)}{\Gamma(3x)^2} [6\psi_0(3x) - 5\psi_0(5x) - \psi_0(x)]. \quad (\text{II.16})$$

Substituting back in for  $x$  and recognizing an occurrence of  $\gamma_2$ , we have the result

$$s_{\gamma_2} = s_\beta \frac{1}{\beta^2} (\gamma_2 + 3) [6\psi_0(3/\beta) - 5\psi_0(5/\beta) - \psi_0(1/\beta)] \quad (\text{II.17})$$

with which we can find the uncertainty in the kurtosis given the value and uncertainty of the shape parameter  $\beta$ .



## **II.6.9 2-D Histograms**

Text goes here.

### **II.6.9.1 Binning and Plotting**

Text goes here.

### **II.6.9.2 Fitting**

Text goes here.

## **II.7 Automation**

Text goes here.

### **II.7.1 Subsection**

Text goes here.

#### **II.7.1.1 Subsubsection**

Text goes here.

#### **II.7.1.2 Subsubsection**

Text goes here.

### **II.7.2 Subsection**

Text goes here.

## CHAPTER III

### Exploring Dark Matter Halo Populations in 2LPT and ZA Simulations

We study the structure and evolution of dark matter halos from  $z = 300$  to  $z = 6$  for two cosmological N-body simulation initialization techniques. While the second order Lagrangian perturbation theory (2LPT) and the Zel'dovich approximation (ZA) both produce accurate present day halo mass functions, earlier collapse of dense regions in 2LPT can result in larger mass halos at high redshift. We explore the differences in dark matter halo mass and concentration due to initialization method through three 2LPT and three ZA initialized cosmological simulations. We find that 2LPT induces more rapid halo growth, resulting in more massive halos compared to ZA. This effect is most pronounced for high mass halos and at high redshift, with a fit to the mean normalized difference between 2LPT and ZA halos as a function of redshift of  $\mu_{\Delta M_{\text{vir}}} = (7.88 \pm 0.17) \times 10^3 z - (3.07 \pm 0.14) \times 10^{-2}$ . Halo concentration is, on average, largely similar between 2LPT and ZA, but retains differences when viewed as a function of halo mass. For both mass and concentration, the difference between typical individual halos can be very large, even for symmetrically distributed quantities, highlighting the shortcomings of ZA-initialized simulations for high- $z$  halo population studies.

#### III.1 Introduction

The pre-reionization epoch is a time of significant evolution of early structure in the universe. Rare density peaks in the otherwise smooth dark matter (DM) sea lead to the collapse and formation of the first dark matter halos. For example, at  $z = 20$ ,  $10^7 M_{\odot}$  halos are  $\sim 4\sigma$  peaks, and  $10^8 M_{\odot}$  halos, candidates for hosting the first supermassive black hole seeds, are  $\sim 5\sigma$  peaks.

These early-forming dark matter halos provide an incubator for the baryonic processes that transform the surrounding space and allow galaxies to form. Initial gas accretion can

lead to the formation of the first Pop-III stars (Couchman & Rees, 1986; Tegmark et al., 1997; Abel et al., 2000, 2002), which, upon their death, can collapse into the seeds for supermassive black holes (SMBHs) (Madau & Rees, 2001; Islam et al., 2003; Alvarez et al., 2009; Jeon et al., 2012) or enrich the surrounding medium with metals through supernovae (Heger & Woosley, 2002; Heger et al., 2003). The radiation from these early quasars (Shapiro & Giroux, 1987; Madau et al., 1999; Fan et al., 2001), Pop-III stars (Gnedin & Ostriker, 1997; Venkatesan et al., 2003; Alvarez et al., 2006), and proto-galaxy stellar populations (Bouwens et al., 2012; Kuhlen & Faucher-Giguère, 2012) all play a key role in contributing to the re-ionizing the universe by around  $z = 6$  (Barkana & Loeb, 2001). Additionally, halo mergers can drastically increase the temperature of halo gas through shock heating, increasing X-ray luminosity (Sinha & Holley-Bockelmann, 2009), and contribute to the unbinding of gas to form the warm-hot intergalactic medium (Bykov et al., 2008; Sinha & Holley-Bockelmann, 2010; Tanaka et al., 2012).

While a number of parameters are required to fully characterize a DM halo, a first-order description can be obtained from its mass and density profile. There are a number of ways to define a halo’s mass. This becomes significant for mass-sensitive studies, such as the halo mass function (Press & Schechter, 1974; Reed et al., 2007; Heitmann et al., 2006; Lukić et al., 2007), the number density of halos as a function of mass and a key probe of cosmology. For a review, see, e.g., White (2001) and references therein. Additionally, see Voit (2005) and references therein for a more observation-focused discussion.

From a simulation standpoint, the two most common ways to obtain halo mass are to define either spherical overdensity halos or friends-of-friends (FOF) halos. The spherical overdensity method identifies regions above a certain density threshold, either with respect to the critical density  $\rho_c = 3H^2/8\pi G$  or the background density  $\rho_b = \Omega_m \rho_c$ , where  $\Omega_m$  is the matter density of the universe. The mass is then the mass enclosed in a sphere of some radius with mean density  $\Delta\rho_c$ , where  $\Delta$  commonly ranges from  $\sim 100$  to  $\sim 500$ . Alternatively, the FOF method finds particle neighbors and neighbors of neighbors defined

to be within some separation distance (Einasto et al., 1984; Davis et al., 1985). Halo mass, then, is simply the sum of the masses of the constituent particles.

The density profile of a DM halo is determined by radially binning the constituent particles into spherical shells, and determining the average density per shell, giving a characteristic  $\rho(r)$ . The most widely used model for the DM halo density profile is the NFW (Navarro et al., 1996) profile

$$\rho(r) = \frac{\rho_0}{\frac{r}{R_s} \left(1 + \frac{r}{R_s}\right)^2}, \quad (\text{III.1})$$

where  $\rho_0$  is the characteristic density, and the scale radius  $R_s$  is the break radius between the inner  $\sim r^{-1}$  and outer  $\sim r^{-3}$  density profiles.

The halo density profile is quantified by the halo concentration  $c \equiv R_{\text{vir}}/R_s$ , where  $R_{\text{vir}}$  is the halo virial radius. Generally, at low redshift, low mass halos are more dense than high mass halos (Navarro et al., 1997a), and concentration decreases with redshift and increases in dense environments (Bullock et al., 2001). Neto et al. (2007) additionally find that concentration decreases with halo mass. Various additional studies have explored concentration's dependence on characteristics of the power spectrum (Eke et al., 2001), cosmological model (Macciò et al., 2008), redshift (Gao et al., 2008; Muñoz-Cuartas et al., 2011), and halo merger and mass accretion histories (Wechsler et al., 2002; Zhao et al., 2003, 2009). For halos at high redshift, Klypin et al. (2011) find that concentration reverses and increases with mass for high mass halos, while Prada et al. (2012) find that concentration's dependence on mass and redshift is more complicated and is better described through  $\sigma(M, z)$ , the rms fluctuation amplitude of the linear density field.

The subtle  $\mathcal{O}(10^{-5})$  density perturbations in place at the CMB epoch are vulnerable to numerical noise and intractable to simulate directly. Instead, a displacement field is applied to the particles to evolve them semi-analytically, nudging them from their initial positions to an approximation of where they should be at a more reasonable starting redshift for the numerical simulation. Starting at a later redshift saves computation time as well as avoiding

interpolation systematics and round-off errors (Lukić et al., 2007).

The Zel’dovich approximation (Zel’dovich, 1970) and 2nd-order Lagrangian Perturbation Theory (Buchert, 1994; Buchert et al., 1994; Bouchet et al., 1995; Scoccimarro, 1998) are the two canonical frameworks for the initial particle displacement involved in generating simulation initial conditions. Zel’dovich approximation (ZA, hereafter) initial conditions (Klypin & Shandarin, 1983; Efstathiou et al., 1985) displace initial particle positions and velocities via a linear field, while 2nd-order Linear Perturbation Theory (2LPT, hereafter) initial conditions (Scoccimarro, 1998; Sirko, 2005; Jenkins, 2010) add a second-order correction term to the expansion of the displacement field.

Following Jenkins (2010), we briefly outline the second-order Lagrangian perturbation theory and compare it to the Zel’dovich approximation. In 2LPT, a displacement field  $\Psi(q)$  is applied to the initial positions  $q$  to yield the Eulerian final comoving positions

$$x = q + \Psi. \quad (\text{III.2})$$

The displacement field is given in terms of two potentials  $\phi^{(1)}$  and  $\phi^{(2)}$  by

$$x = q - D_1 \nabla_q \phi^{(1)} + D_2 \nabla_q \phi^{(2)}, \quad (\text{III.3})$$

with linear growth factor  $D_1$  and second-order growth factor  $D_2 \approx -3D_1^2/7$ . The subscripts  $q$  refer to partial derivatives with respect to the Lagrangian coordinates  $q$ . Likewise, the comoving velocities are given, to second order, by

$$v = -D_1 f_1 H \nabla_q \phi^{(1)} + D_2 f_2 H \nabla_q \phi^{(2)}, \quad (\text{III.4})$$

with Hubble constant  $H$  and  $f_i = d \ln D_i / d \ln a$ , with expansion factor  $a$ . The relations  $f_1 \approx \Omega^{5/9}$  and  $f_2 \approx 2\Omega^{6/11}$ , with matter density  $\Omega$ , apply for flat models with a non-zero cosmological constant (Bouchet et al., 1995). The  $f_1$ ,  $f_2$ , and  $D_2$  approximations here are

very accurate for most actual  $\Lambda$ CDM initial conditions, as  $\Omega$  is close to unity at high starting redshift (Jenkins, 2010). We may derive  $\phi^{(1)}$  and  $\phi^{(2)}$  by solving a pair of Poisson equations

$$\nabla_q^{(1)}(q) = \delta^{(1)}(q), \quad (\text{III.5})$$

with linear overdensity  $\delta^{(1)}(q)$ , and

$$\nabla_q^{(2)}(q) = \delta^{(2)}(q). \quad (\text{III.6})$$

The second order overdensity  $\delta^{(2)}(q)$  is related to the linear overdensity field by

$$\delta^{(2)}(q) = \sum_{i>j} \left\{ \phi_{,ii}^{(1)}(q) \phi_{,jj}^{(1)}(q) - \left[ \phi_{,ij}^{(1)}(q) \right]^2 \right\}, \quad (\text{III.7})$$

where  $\phi_{,ij} \equiv \partial^2 \phi / \partial q_i \partial q_j$ . For initial conditions from the Zel’dovich approximation, or first-order Lagrangian initial conditions, the  $\phi^{(2)}$  terms of Equations III.3 and III.4 are ignored.

Cosmological simulations that follow the initial collapse of dark matter density peaks into virialized halos often neglect to consider the nuances of initialization method. Non-linear decaying modes, or transients, will be damped as  $1/a$  in ZA. In 2LPT, however, transients are damped more quickly as  $1/a^2$ . It should be expected, then, that structure in 2LPT will be accurate after fewer  $e$ -folding times than in ZA (Scoccimarro, 1998; Crocce et al., 2006; Jenkins, 2010). The practical result is that high- $\sigma$  DM density peaks at high redshift are suppressed in ZA compared with 2LPT for a given starting redshift (Crocce et al., 2006).

While differences in ensemble halo properties, such as the halo mass function, between simulation initialization methods are mostly washed away by  $z = 0$  (Scoccimarro, 1998), trends at earlier redshifts are less studied (Lukić et al., 2007). In this paper, we explore the effects of ZA and 2LPT on the evolution of halo populations at high redshift. It is thought that 2LPT allows initial DM overdensities to get a “head start” compared with ZA, allowing

earlier structure formation, more rapid evolution, and larger possible high-mass halos for a given redshift. We explore this possibility by comparing halo properties in (otherwise identical) simulations initialized with ZA and 2LPT.

We discuss the simulations, halo finding, and analysis methods in Section III.2, results in Section III.3, implications, caveats, and future work in Section III.4, and finally summarize our results and conclude in Section IV.4.

### III.2 Numerical Methods

We use the Nbody tree/SPH code GADGET-2 (Springel et al., 2001; Springel, 2005) to evolve six dark matter-only cosmological volumes from  $z_{\text{start}} = 300$  to  $z = 6$  in a  $\Lambda$ CDM universe. Each simulation is initialized using WMAP-5 (Komatsu et al., 2009) parameters. For each of the three simulation pairs, we directly compare 2LPT and ZA by identically sampling the CMB transfer function and displacing the initial particle positions to the same starting redshift using 2LPT and ZA. The three sets of simulations differ only by the initial phase sampling random seed. Each volume contains  $512^3$  particles in a  $10 h^{-1}$  Mpc box. Full simulation details are discussed in Holley-Bockelmann et al. (2012).

One facet often overlooked when setting up an N-body simulation is an appropriate starting redshift, determined by box size and resolution (Lukić et al., 2007). Initialization with 2LPT allows for a later starting redshift compared with an equivalent ZA-initialized simulation. However, many ZA simulations do not take this into account, starting from too late of an initial redshift (Crocce et al., 2006; Jenkins, 2010). In order to characterize an appropriate starting redshift, the relation between the initial rms particle displacement and mean particle separation must be considered. The initial rms displacement  $\Delta_{\text{rms}}$  is given by

$$\Delta_{\text{rms}}^2 = \frac{4\pi}{3} \int_{k_f}^{k_{\text{Ny}}} P(k, z_{\text{start}}) dk, \quad (\text{III.8})$$

where  $k_f = 2\pi/L_{\text{box}}$  is the fundamental mode,  $L_{\text{box}}$  is the simulation box size,  $k_{\text{Ny}} = \frac{1}{2}Nk_f$  is the Nyquist frequency of an  $N^3$  simulation, and  $P(k, z_{\text{start}})$  is the power spectrum at

starting redshift  $z_{\text{start}}$ . In order to avoid the “orbit crossings” that reduce the accuracy of the initial conditions,  $\Delta_{\text{rms}}$  must be some factor smaller than the mean particle separation  $\Delta_p = L_{\text{box}}/N$  (Holley-Bockelmann et al., 2012). For example, making orbit crossing a  $\sim 10\sigma$  event imposes  $\Delta_{\text{rms}}/\Delta_p = 0.1$ . However, for small-volume, high-resolution simulations, this quickly leads to impractical starting redshifts. Continuing our example, satisfying  $\Delta_{\text{rms}}/\Delta_p \sim 0.1$  for a  $10h^{-1}$  Mpc,  $512^3$  simulation suggests  $z_{\text{start}} \approx 799$ . Starting at such a high redshift places such a simulation well into the regime of introducing errors from numerical noise caused by roundoff errors dominating the smooth potential. A more relaxed requirement of  $\Delta_{\text{rms}}/\Delta_p = 0.25$  yields  $z_{\text{start}} = 300$ , which we adopt for this work.

For each of our six simulations, we use the 6-D phase space halo finder code ROCKSTAR (Behroozi et al., 2013) to identify spherical overdensity halos at each timestep. ROCKSTAR follows an adaptive hierarchical refinement of friends-of-friends halos in 6-D phase space, allowing determination of halo properties such as halo mass, position, virial radius, internal energy, and number of subhalos. ROCKSTAR tracks halos down to a threshold of around 20 particles, but we use a more conservative 100 particle threshold for our analysis. We use all particles found within the virial radius to define our halos and their properties.

We identify matching halos based on the highest fraction of matching particles contained in each at any given timestep. We remove subhalo matches (i.e. a halo must not be contained within another halo) and halo pairs with fewer than 100 particles in either 2LPT or ZA. We are left with approximately 60,000 total halo pairs for our three boxes at  $z = 6$ . With halo catalogues matched between simulations, we can compare properties of individual corresponding halos. To mitigate the effects of cosmic variance on our small volumes, we “stack” the three simulation boxes for each initialization method, and combine the halos from each into one larger sample in our analysis.

Halo concentration is derived from ROCKSTAR’s output for  $R_s$  and  $R_{\text{vir}}$ . Here,  $R_{\text{vir}}$  is the virial radius as defined by Bryan & Norman (1998). Figure III.1 makes evident the difficulty in fitting density profiles and obtaining concentration measurements for typical



realistic halos. Large substructure, as displayed by the ZA halo, can disrupt the radial symmetry of the halo and cause significant deviations in the density profile. Centering can also be an issue in these cases. Due to these complications, there are a number of approaches for finding halo concentrations (Prada et al., 2012), but for consistency, we use the values derived from ROCKSTAR’s fitting for our concentration measurements.

At each simulation snapshot, we measure and compare a number of parameters for halos in both 2LPT and ZA simulations. For each quantity  $q$ , we create histograms of  $\Delta q$ , the normalized difference in  $q$  between halos in the 2LPT and ZA simulations, defined as

$$\Delta q = \frac{q_{2\text{LPT}} - q_{\text{ZA}}}{q_{\text{avg}}}, \quad (\text{III.9})$$

where  $q_{\text{avg}} = \frac{1}{2}(q_{2\text{LPT}} + q_{\text{ZA}})$ . For each of these, we fit the  $\Delta q$  histograms with a generalized normal distribution (Nadarajah, 2005) with the probability density function

$$f(x) = \frac{\beta}{2\alpha\Gamma(1/\beta)} e^{-(|x-\mu|/\alpha)^\beta}, \quad (\text{III.10})$$

where  $\mu$  is the mean,  $\alpha$  is the scale parameter,  $\beta$  is the shape parameter, and  $\Gamma$  is the gamma function

$$\Gamma(t) = \int_0^\infty x^{t-1} e^{-x} dx. \quad (\text{III.11})$$

The shape parameter  $\beta$  is restricted to  $\beta \geq 1$ . This allows the distribution to potentially vary from a Laplace distribution ( $\beta = 1$ ) to a uniform distribution ( $\beta = \infty$ ) and includes the normal distribution ( $\beta = 2$ ). The distribution has variance

$$\sigma^2 = \frac{\alpha^2 \Gamma(3/\beta)}{\Gamma(1/\beta)} \quad (\text{III.12})$$

and excess kurtosis

$$\gamma_2 = \frac{\Gamma(5/\beta)\Gamma(1/\beta)}{\Gamma(3/\beta)^2} - 3. \quad (\text{III.13})$$

The distribution is symmetric, and thus has no skewness by definition. As such, the values for skew presented below are measured directly from the data.

As our fitting distributions are symmetrical and skew must therefore be measured directly from the data, in order to derive uncertainties for skew, we measure the skew of the distributions for each of our three simulation boxes individually as well as for the single stacked data set. Uncertainty in skew is then simply the standard deviation of the mean of the skew of the three individual boxes.

Determining the uncertainty in the kurtosis is slightly more involved, as kurtosis is determined by a transformation of the generalized normal distribution's shape parameter  $\beta$  according to Equation III.13. Following the standard procedure for propagation of uncertainty, we calculate the standard deviation of the kurtosis as

$$s_{\gamma_2} = \sqrt{\left(\frac{d\gamma_2}{d\beta}\right)^2 s_{\beta}^2} \quad (\text{III.14})$$

$$= s_{\beta} \frac{d}{d\beta} \left[ \frac{\Gamma(5/\beta)\Gamma(1/\beta)}{\Gamma(3/\beta)^2} - 3 \right]. \quad (\text{III.15})$$

The derivative of the gamma function is

$$\Gamma'(x) = \Gamma(x)\psi_0(x), \quad (\text{III.16})$$

where the digamma function  $\psi_0$  is the derivative of the logarithm of the gamma function and is given by

$$\psi_0(x) = \int_0^{\infty} \left( \frac{e^{-t}}{t} - \frac{e^{-xt}}{1-e^{-t}} \right) dt \quad (\text{III.17})$$

if the real part of  $x$  is positive. Now, taking the derivative of  $\gamma_2$  and doing a bit of algebra gives us

$$s_{\gamma_2} = s_{\beta} \frac{1}{\beta^2} (\gamma_2 + 3) [6\psi_0(3/\beta) - 5\psi_0(5/\beta) - \psi_0(1/\beta)], \quad (\text{III.18})$$

with which we can find the uncertainty in the kurtosis given the value and uncertainty of

the shape parameter  $\beta$  estimated from the least squares fit routine.

In addition to distributions of  $\Delta q$ , we also consider distributions of

$$\Delta'q = \frac{q_{2\text{LPT}} - q_{\text{ZA}}}{q_{\text{ZA}}} \quad (\text{III.19})$$

in order to better quantify the fraction of halos differing by a given amount between 2LPT and ZA simulations. This distribution is inherently non-symmetrical, and is only defined for  $\Delta'q \geq -1$  for positive quantities like mass and concentration. In order to consider halo pairs that differ by a certain amount in either direction (e.g. pairs that differ by 10%, whether larger in 2LPT or ZA), a relation for equivalent displacement is required. Rearranging Equation III.19 yields

$$q_{2\text{LPT}} = (\Delta'q + 1)q_{\text{ZA}}, \quad (\text{III.20})$$

and making the substitution  $x = \Delta'q + 1$  gives us

$$q_{2\text{LPT}} = xq_{\text{ZA}}. \quad (\text{III.21})$$

For a given  $x_1$ , we want an  $x_2$  such that  $x_2 = 1/x_1$ . Substituting now for  $x_1$  and  $x_2$  and rearranging gives us

$$\Delta'q_2 = \frac{1}{\Delta'q_1 + 1} - 1, \quad (\text{III.22})$$

the value for which a halo pair with a larger  $q$  in ZA would differ by the same factor as a halo pair with a larger  $q$  in 2LPT where  $\Delta'q = \Delta'q_1$ .

### III.3 Results

With our catalog of matched dark matter halos, we directly compare differences in halo properties arising from initialization with 2LPT vs ZA. We consider halos on a pair-by-pair basis as well as the entire sample as a whole. Overall, we find 2LPT halos undergo more growth at a given redshift than their ZA counterparts.

### III.3.1 Individual halo pairs

We compare large scale morphologies, density profiles, and various other halo properties for halo pairs on an individual halo-by-halo basis for several of the most massive halos. Morphologies appear similar for most halos, indicating good halo matches between simulations. However, many pairs display differences in central morphology, such as the number and separation of central density peaks. We interpret these cases to be examples of differences in merger epochs, in which case one halo may still be undergoing a major merger, while its companion is in a more relaxed post-merger state. We give an example of one such pair at  $z = 6$  in Figure III.1. The top two rows show density projections of the nuclear regions for a large 2LPT and matching ZA halo (first and second rows, respectively). We find the ZA halo to contain two distinct density peaks with a separation of  $\sim 10$  kpc, while the 2LPT halo displays only a single core. On the third and fourth rows, we plot the density profiles of the same two halos (2LPT and ZA, respectively). Here, with nearly identical virial radii, it is readily seen that the 2LPT halo is more concentrated than the ZA halo.

### III.3.2 Difference distributions of halo properties

For the halo population as a whole, we consider distributions of halo virial mass  $M_{\text{vir}}$  and concentration  $c$ . We plot histograms of  $\Delta M_{\text{vir}}$  and  $\Delta c$  in the left and right columns, respectively, of Figure III.2 for three representative timesteps at redshifts of  $z = 14.7$ ,  $z = 10.3$ , and  $z = 6.0$ . For each panel, the blue histogram features the entire halo sample, and the smaller gray-filled green histogram displays only the top 25% most massive halos, ordered by 2LPT mass. Fits to the primary histograms are overplotted as red dashed curves.

Throughout the simulation, we find a tendency for 2LPT halos to be more massive. At  $z = 15$ , the mean of the  $\Delta M_{\text{vir}}$  distribution is  $(9.3 \pm 1.2) \times 10^{-2}$ . The mean is consistently positive (heavier 2LPT halos) and is most displaced from zero at high redshift. The peak of the distribution gradually moves closer to zero as we progress in redshift. We find the least difference between paired halos for the final snapshot at  $z = 6$ , with  $\mu_{\Delta M_{\text{vir}}} =$

$$(1.79 \pm 0.31) \times 10^{-2}.$$

The higher-order moments of the  $\Delta M_{\text{vir}}$  distribution are of interest as well, as we find significant deviation from a Gaussian distribution. As we use the symmetrical generalized normal distribution as our fit function, the skewness of the data is unable to be measured from the fit itself. However, a qualitative deviation from symmetry can be readily observed. By  $z = 6$ , we end up with a rather symmetrical distribution, with both sides of the histogram equally well described by our fit. However, at higher redshift, we note a marked increase in skewness and deviation from this symmetry. As redshift increases, we observe an increasing difference between the fit curve and the bins to the left of the histogram peak.

We find the distributions to be much closer to a Laplace distribution than a Gaussian, with shape parameter consistently sitting at or very close to  $\beta = 1$ . Compared to a Gaussian distribution, the larger excess kurtosis implies a narrower central peak and heavier outlying tails. Our fit constrains  $\beta \geq 1$ , so the kurtosis of the data itself could potentially be higher than the fit implies.

We find no overall preference for more concentrated 2LPT or ZA halos. In contrast to the  $\Delta M_{\text{vir}}$  histograms,  $\Delta c$  shows very little deviation from symmetry about zero. Throughout the simulation, we find the distributions to have a mean close to zero and negligible skew. The widths of the distributions are much wider than those for  $\Delta M_{\text{vir}}$ , with an order of magnitude difference by  $z = 6$ . As with mass, concentration histograms are sharply peaked with heavy tails, implying a tendency for halo pairs to move towards the extremes of either very similar or very discrepant concentrations.

### III.3.3 Trends with redshift

In Figure III.3, we more quantitatively assess the evolution of our various trends hinted at in Figure III.2. Here, we plot the mean, root mean square (RMS), standard deviation, skew, and kurtosis for  $\Delta M_{\text{vir}}$  and  $\Delta c$  as functions of redshift. Uncertainty in the mean is estimated directly by the least squares fitting routine.

Table III.1: Coefficients for linear least squares fits from Figure III.3.

	$\Delta M_{\text{vir}}$	$\Delta c$
A	$(7.88 \pm 0.17) \times 10^{-3}$	$(3.62 \pm 0.95) \times 10^{-3}$
B	$(-3.07 \pm 0.14) \times 10^{-2}$	$(-2.34 \pm 0.84) \times 10^{-2}$

The mean for  $\Delta M_{\text{vir}}$  is positive and highest at high redshift, trending toward zero by the end of the simulation. Distributions for  $\Delta c$  retain means close to and consistent with zero. Standard deviation decreases slightly for both  $\Delta M_{\text{vir}}$  and  $\Delta c$ . From  $z = 15$  to  $z = 6$ , standard deviation falls from  $(9.0 \pm 1.5) \times 10^{-2}$  to  $(6.08 \pm 0.31) \times 10^{-2}$  for  $\Delta M_{\text{vir}}$  and from  $0.73 \pm 0.11$  to  $0.551 \pm 0.026$  for  $\Delta c$ .

We find least square linear fits for both mean  $\Delta M_{\text{vir}}$  vs  $z$  and mean  $\Delta c$  vs  $z$ . Coefficients for slope  $A$  and y-intercept  $B$  for the fit equation  $\mu = Az + B$  are given in Table III.1 for both cases. We find a significant trend for  $\Delta M_{\text{vir}}$ , with a slope  $\sim 46\sigma$  from zero. Conversely, the slope for  $\Delta c$  is much smaller and, considering the larger spread of the underlying distributions, can be considered negligible. For  $\Delta M_{\text{vir}}$ , the y-intercept coefficient  $B$  likely has little meaning in terms of the actual behavior at  $z = 0$ , as we expect the trend to level out at later redshift.

We do note, however, that the mean can be deceiving as an indicator of total difference between halo populations, especially when it is close to zero as with concentration. It should be noted that while the mean can indicate a lack of average difference between the whole sample of 2LPT and ZA halos, there can still be very large discrepancies between many individually paired halos. We visualize this by plotting the RMS of  $\Delta M_{\text{vir}}$  and  $\Delta c$ , which is plotted as a green dotted line. Unlike the mean, standard deviation, and kurtosis, which are measured from fits to the histograms, RMS is measured directly from the data and is not dependent on fitting. The large RMS values are indicative of how much overall difference can arise between 2LPT and ZA halos, even though the differences may average to zero when considering the entire population. The RMS for both  $\Delta M_{\text{vir}}$  and  $\Delta c$  starts highest at high redshift—0.19 for  $\Delta M_{\text{vir}}$  and 0.57 for  $\Delta c$  at  $z = 15$ —and steadily decreases

throughout the simulation, reaching minimums of 0.11 for  $\Delta M_{\text{vir}}$  and 0.45 for  $\Delta c$  by  $z = 6$ .

Additionally, it is of interest to consider the percentage of halo pairs that are “wrong” at some given time, regardless of whether the quantity is higher in 2LPT or ZA. For example, if we count halos outside a slit of  $\varepsilon = 10\%$  around  $\Delta q = 0$ , we find that by  $z = 6$ , 14.6% of halo pairs still have substantially mismatched masses, and 74.3% have mismatched concentrations. It is evident that a substantial percentage of halo pairs can have markedly different growth histories, even when there is little or no offset in the ensemble halo population average.

Kurtosis is consistently large for both mass and concentration, with a slight increasing trend throughout the simulation for concentration. It reaches maximum values of  $17.5 \pm 2.4$  at redshift 10 for  $\Delta M_{\text{vir}}$  and  $15.4 \pm 1.0$  at the end of the simulation at redshift 6 for  $\Delta c$ . Skew is positive for much of the simulation for mass, but is much smaller for concentration. We find average skews of  $0.39 \pm 0.29$  for  $\Delta M_{\text{vir}}$  and  $0.045 \pm 0.028$  for  $\Delta c$ . These higher moment deviations from Gaussianity hint at the non-linear dynamics at play in halo formation.

The narrow peak and heavy tails of the distribution may indicate a fair amount of sensitivity to initial differences in halo properties, in that halo pairs that start out within a certain range of the mean are more likely move closer to the mean, while pairs that are initially discrepant will diverge even further in their characteristics. This is indicative of the non-linear gravitational influence present during halo evolution, and is further supported by a kurtosis that increases with time.

The skew at high redshift for  $\Delta M_{\text{vir}}$  may give another hint at the non-linear halo formation process. Runaway halo growth causes more massive halos to favor faster mass accretion and growth. The positively skewed distributions show a picture of 2LPT halo growth in which initial differences in mass are amplified the most readily in the earliest forming and most massive halos, again indicating the extra kick-start to halo growth provided by 2LPT initialization. While the slight decrease in skew with redshift may be counter-intuitive to this notion, it is likely that the large number of newly formed halos begin to mask the signal

from the smaller number of large halos displaying this effect.

### III.3.4 Trends with halo mass

We consider  $\Delta M_{\text{vir}}$  and  $\Delta c$  as a function of average halo mass  $M_{\text{vir,avg}} = (M_{\text{vir,2LPT}} + M_{\text{vir,ZA}})/2$  in Figure III.4. The data is binned on a 2-D grid with a logarithmic color map for three representative timesteps. A linear fit to the data is overplotted in red, and a dotted blue line is provided at  $\Delta M_{\text{vir}} = 0$  and  $\Delta c = 0$  to guide the eye.

We find that  $\Delta M_{\text{vir}}$  tends to increase with increasing  $M_{\text{vir,avg}}$ , a trend that is, again, most pronounced at high redshift. 2LPT halos are consistently more massive than their ZA counterparts, with the difference increasing with average halo mass. While less massive halo pairs have a larger spread in the difference in 2LPT and ZA mass, more massive halo pairs are consistently heavier in 2LPT than in ZA. At redshift 15, the least squares fit to the data produces the fit equation  $\Delta M_{\text{vir}} = 5.6 \times 10^{-2} M_{\text{vir,avg}} - 0.33$ . The slope of the fit line trends towards zero as we progress in redshift, with little average mass dependence and a fit of  $\Delta M_{\text{vir}} = 6.4 \times 10^{-3} M_{\text{vir,avg}} - 2.5 \times 10^{-2}$  by  $z = 6$ .

We find a small trend for more massive halo pairs to be more concentrated in ZA, but this trend is weaker than for  $\Delta M_{\text{vir}}$ . The fit equations for  $z = 15$  and  $z = 6$  are  $\Delta c = -5.3 \times 10^{-2} M_{\text{vir,avg}} - 0.45$  and  $\Delta c = -9.3 \times 10^{-3} M_{\text{vir,avg}} - 8.9 \times 10^{-2}$ , respectively. The negative slope might be expected, as halo concentration is expected to decrease with increasing mass, at least at later redshift (Neto et al., 2007), and we find high mass halos to be more massive in 2LPT than in ZA. However, the dependence of concentration on mass and redshift at high redshift is more complicated (Klypin et al., 2011; Prada et al., 2012). The data have a larger variance than  $\Delta M_{\text{vir}}$ , and fits have an overall shallower slope. Mass dependence all but disappears by  $z = 6$ . To reconcile these trends with the symmetrical concentration distributions of Figure III.2, we note that the trends in mass may be hidden by integration across the entire mass range and still result in overall  $\Delta c$  distributions symmetric about zero.



### III.3.5 Alternate fractional difference distributions

In Figure III.5, we plot, as functions of redshift, statistics derived from the alternate fractional difference distributions  $\Delta' M_{\text{vir}}$  and  $\Delta' c$  (see Equation III.19). In the left column, we plot the  $\Delta' q$  of the peak of the distribution along with the  $\Delta' q$  where various percentages of the halo pairs fall at or above  $\Delta' q$ .

As the  $\Delta' q$  value of peak of the distribution is the location of the mode, it represents the most typical halo pair. While concentration differences remain close to zero throughout the simulation, mass difference peak moves from a  $\Delta' M_{\text{vir}}$  of  $8.7 \times 10^{-2}$  at  $z = 15$  to  $2.9 \times 10^{-2}$  at  $z = 6$ . The 1% of halo pairs with the largest excess 2LPT mass are at least 1.97 times ZA mass at  $z = 15$  and 1.45 times ZA mass at  $z = 6$ . For concentration, the 1% most 2LPT concentrated halo pairs differ by at least a factor of 6.00 at  $z = 15$  and 3.73 at  $z = 6$ .

In the right column of Figure III.5, we plot the fraction of halos  $f_h$  that fall outside various  $\Delta' q$  values. The solid lines represent halo pairs that have  $\Delta' q$  greater than or equal to the listed values, i.e., the fraction of halo pairs where the 2LPT halo has a virial mass or concentration that is at least 1.1, 1.5, 2.0, or 5.0 times that of its corresponding ZA halo. The dashed lines additionally count halos with  $\Delta' q$  at or below the corresponding equivalent displacement (see Equation III.22) and represent the fraction of halo pairs where one halo has a virial mass or concentration at least 1.1, 1.5, 2.0, or 5.0 times that of its companion, regardless of whether the 2LPT or ZA value is higher.

We find that 50% of halo pairs are at least 10% more massive in 2LPT at  $z = 15$ . By  $z = 6$ , this has fallen to 10%. Furthermore, 0.81% are at least twice as massive in 2LPT at  $z = 15$ , and by  $z = 6$ , this has only reduced to 0.26%. Halos in 2LPT are at least twice as concentrated as their ZA counterparts for at least 12% of the halo population at  $z = 15$  and at least 7.8% of the population by  $z = 6$ . Halo pairs that are at least 5 times as concentrated in 2LPT make up 1.3% at  $z = 15$  and 0.26% at  $z = 6$ .

When we additionally consider halo pairs that are less than or equal to the equivalent displacement, i.e. pairs where either the 2LPT or ZA halos has the higher mass or concen-

tration, we include an even larger percentage of the population. We find 54% of the halo pairs differ in mass by at least 10% at  $z = 15$ , with 16% differing by  $z = 6$ . Halos that are at least twice as massive in either 2LPT or ZA account for 1.1% at  $z = 15$  and 0.46% at  $z = 6$ . Halos that are at least twice as concentrated in either 2LPT or ZA account for 25% at  $z = 15$  and 15% at  $z = 6$ .

### III.4 Discussion

As we evolve our DM halo population from our initial redshift to  $z = 6$ , we find that simulation initialization with 2LPT can have a significant effect on halo population compared to initialization with ZA. The second order displacement boost of 2LPT provides a head start on the initial collapse and formation of DM halos. This head start manifests itself further along in a halo's evolution as more rapid growth and earlier mergers. 2LPT halos are, on average, more massive than their ZA counterparts, with a maximum mean  $\Delta M_{\text{vir}}$  of  $(9.3 \pm 1.2) \times 10^{-2}$  at  $z = 15$ . The larger mass for 2LPT halos is more pronounced for higher mass pairs, while 2LPT halo concentration is larger on the small mass end. Both mass and concentration differences trend towards symmetry about zero as halos evolve in time, with the smallest difference observed at the end of the simulations at  $z = 6$ , with a mean  $\Delta M_{\text{vir}}$  of  $(1.79 \pm 0.31) \times 10^{-2}$ . Casual extrapolation of our observed trends with redshift to today would indicate that, barring structure like massive clusters that form at high redshift, 2LPT and ZA would produce very similar halo populations by  $z = 0$ . However, the larger differences at high redshift should not be ignored.

The earlier formation times and larger masses of halos seen in 2LPT-initialized simulations could have significant implications with respect to early halo life during the Dark Ages. Earlier forming, larger halos affect the formation of Pop-III stars, and cause SMBHs to grow more rapidly during their infancy (Holley-Bockelmann et al., 2012). The epoch of peak star formation may also be shifted earlier. This could additionally affect the contribution of SMBHs and early star populations to re-ionization. Larger halos may also influence

studies of the high- $z$  halo mass function, abundance matching, gas dynamics, AGN, clustering, and large scale structure formation.

In these discussions, it is important to note that it is wrong to assume that the ZA halo properties are the “correct” halo properties, even in a statistical sense. While halo mass suggests the most obvious shortcoming of ZA simulations, even properties such as concentration—that show little difference on average between 2LPT and ZA—can have large discrepancies on an individual halo basis. Failure to consider uncertainties in halo properties for high  $z$  halos in ZA simulations can lead to catastrophic errors.

We note a few caveats with our simulations and analysis. We did not exclude substructure when determining the properties of a halo, and although this would not change the broad conclusions herein, care must be taken when comparing to works which remove subhalo particles in determining halo mass and concentration. Halo matching is not perfect, as it is based on one snapshot at a time, and may miss count halos due to merger activity and differences in merger epochs. However, we believe this effect to be minor. While we compared ROCKSTAR’s output with our own fitting routines and found them to be in good agreement, ROCKSTAR does not provide goodness of fit parameters for its NFW profile fitting and  $R_s$  measurements. It also may be debated whether it makes sense to even consider concentration of halos at high redshift which are not necessarily fully virialized.

ROCKSTAR does not provide goodness-of-fit parameters for its internal density profile measurements used to derive concentration, so error estimates for concentration values of individual halos are unknown. Additionally, proper density profile fitting is non-trivial, as the non-linear interactions of numerical simulations rarely result in simple spherical halos that can be well described using spherical bins.

We use a simulation box size of only  $(10 \text{ Mpc})^3$ . This is too small to effectively capture very large outlier density peaks. We would, however, expect these large uncaptured peaks to most affected by 2LPT initialization, so the effects presented here may even be dramatically underestimated. Additionally, a larger particle number would allow us to consider smaller

mass halos than we were able to here, and to better resolve all existing structure. A higher starting redshift could probe the regime where 2LPT initialization contributes the most. It would also be of interest to evolve our halo population all the way to  $z = 0$ . The addition of baryons in a fully hydrodynamical simulation could also affect halo properties. These points may be address in future studies.

### III.5 Conclusion

We analyzed three 2LPT and ZA simulation pairs and tracked the spherical overdensity dark matter halos therein with the 6-D phase space halo finder code ROCKSTAR to compare the effect of initialization technique on properties of particle–matched dark matter halos. This approach allowed us to directly compare matching halos between simulations and isolate the effect of using 2LPT over ZA. In summary, we found the following:

- 2LPT halos get a head start in the formation process and grow faster than their ZA counterparts. Companion halos in 2LPT and ZA simulations may have offset merger epochs and differing nuclear morphologies.
- 2LPT halos are, on average, more massive than ZA halos. At  $z = 15$ , the mean of the  $\Delta M_{\text{vir}}$  distribution is  $(9.3 \pm 1.2) \times 10^{-2}$ , and 50% of 2LPT halos are at least 10% more massive than their ZA companions. By  $z = 6$ , the mean  $\Delta M_{\text{vir}}$  is  $(1.79 \pm 0.31) \times 10^{-2}$ , and 10% of 2LPT halos are at least 10% more massive.
- This preference for more massive 2LPT halos is dependent on redshift, with the effect most pronounced at high  $z$ . This trend is best fit by  $\Delta M_{\text{vir}} = (7.88 \pm 0.17) \times 10^{-3} z - (3.07 \pm 0.14) \times 10^{-2}$ .
- Earlier collapse of the largest initial density peaks causes the tendency for more massive 2LPT halos to be most pronounced for the most massive halos, especially at high  $z$ . We find a trend of  $\Delta M_{\text{vir}} = 5.6 \times 10^{-2} M_{\text{vir,avg}} - 0.33$  for  $z = 15$ . By  $z = 6$ , this has flattened to  $\Delta M_{\text{vir}} = 6.4 \times 10^{-3} M_{\text{vir,avg}} - 2.5 \times 10^{-2}$ .

- Halo concentration, on average, is similar for 2LPT and ZA halos. However, even by the end of the dark ages, the width of the  $\Delta c$  distribution— $\sigma_{\Delta c} = 0.551 \pm 0.026$  at  $z = 6$ —is large and indicative of a significant percentage of halos with drastically mismatched concentrations, despite the symmetrical distribution of  $\Delta c$ . At  $z = 15$ , 25% of halo pairs have at least a factor of 2 concentration difference, with this falling to 15% by  $z = 6$ .
- There is a slight trend for ZA halos to be more concentrated than 2LPT halos at high mass. We find  $\Delta c = -5.3 \times 10^{-2} M_{\text{vir,avg}} - 0.45$  at  $z = 15$  and  $\Delta c = -9.3 \times 10^{-3} M_{\text{vir,avg}} - 8.9 \times 10^{-2}$  at  $z = 6$ . This is not visible in the symmetrical  $\Delta c$  distributions, as the trends are roughly centered about zero and are washed away when integrated across the entire mass range.

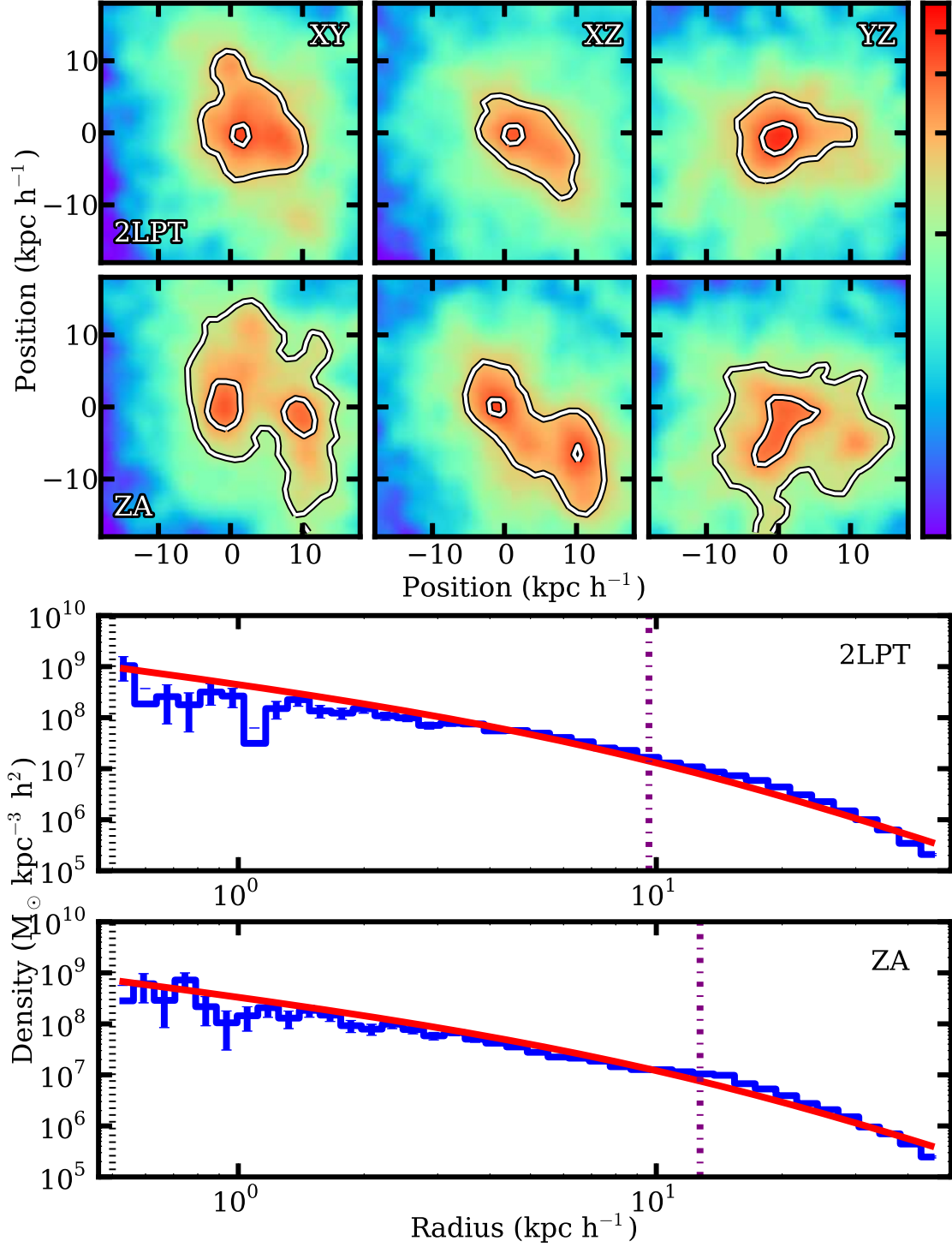


Figure III.1: *Top two rows:* Density projections for two matching halos at  $z = 6$ . The first and second row are 2LPT and ZA, respectively. The halos appear to be either undergoing or have recently undergone a major merger. The 2LPT halo appears to be more relaxed and further along in the merger process, while the ZA halo lags behind, still displaying two distinct cores. The halos have masses of  $5.95 \times 10^9 M_{\odot}$  for 2LPT and  $5.85 \times 10^9 M_{\odot}$  for ZA. *Bottom two rows:* Density profiles for the same two halos as above. NFW profiles are fit to logarithmic radial bins of particle position and are overplotted as red curves. The purple dot-dash lines mark the scale radii. The black dotted lines mark the resolution limit of the simulations.

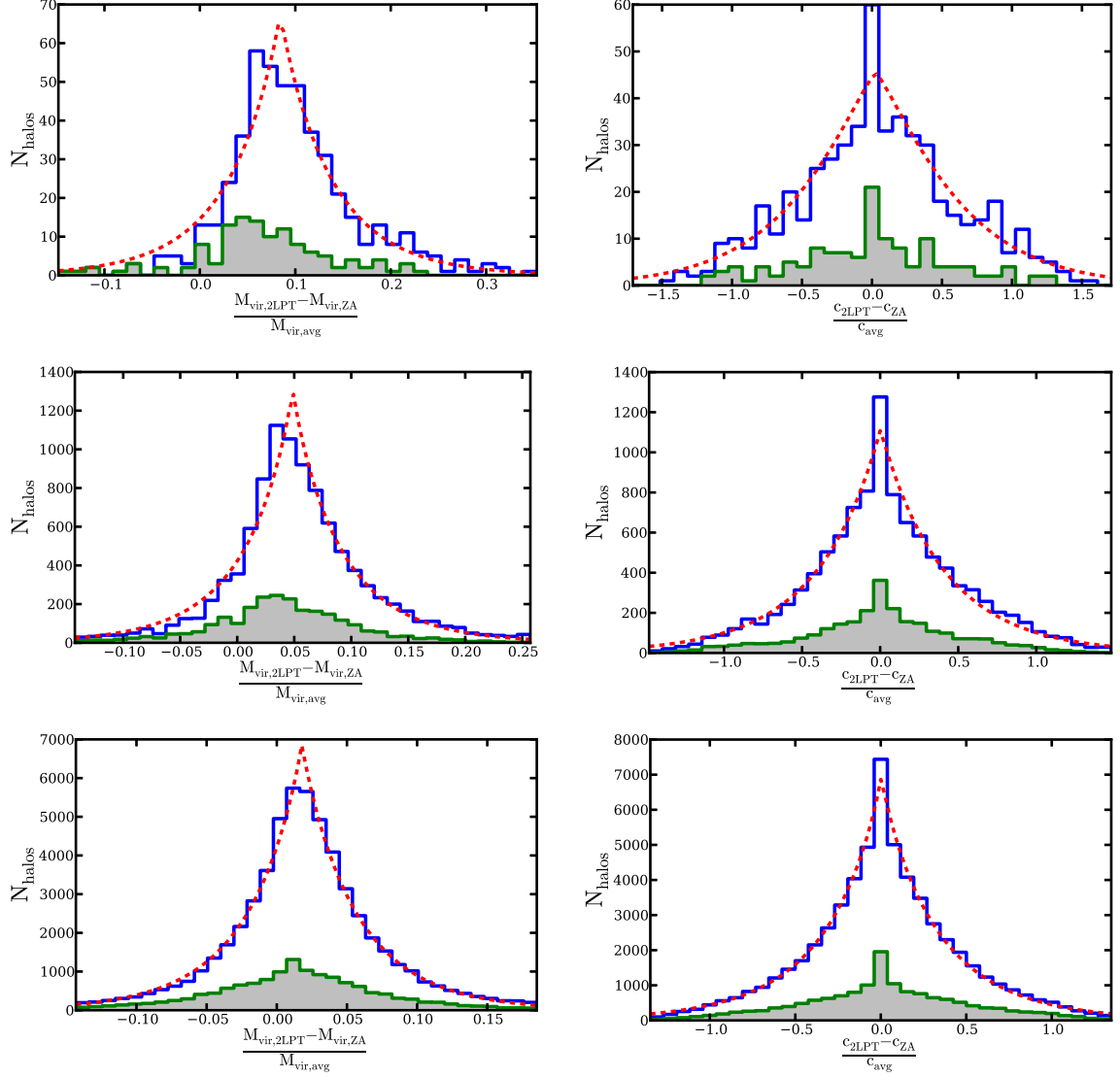


Figure III.2: Histograms of  $\Delta M_{\text{vir}}$  (left column) and  $\Delta c$  (right column) for snapshots at  $z = 14.7$ ,  $z = 10.3$ , and  $z = 6.0$  (top, middle, and bottom panels, respectively). The small gray-filled histograms count only the top 25% most massive halos. The main histograms are fit with a generalized normal distribution with parameters for mean, scale, and shape, overplotted as the red dashed line (see Equation III.10). The distributions for  $\Delta M_{\text{vir}}$  have positive means and heavier 2LPT halos, with the most pronounced difference at high redshift. The distributions shown here have means of  $(8.4 \pm 1.8) \times 10^{-2}$ ,  $(4.87 \pm 0.87) \times 10^{-2}$ , and  $(1.79 \pm 0.31) \times 10^{-2}$ , respectively. The skew of the distribution is also the most positive at high redshift, and shifts toward symmetry by  $z = 6$ . The  $\Delta c$  distributions remain symmetric about zero and have negligible skew. The means are consistent with zero, at  $(2.6 \pm 2.7) \times 10^{-2}$ ,  $(0.2 \pm 2.6) \times 10^{-2}$ , and  $(0.3 \pm 1.1) \times 10^{-2}$ , respectively. Both distributions have excess kurtosis consistently larger than that of a standard Gaussian distribution, with a sharp peak and heavy tails.

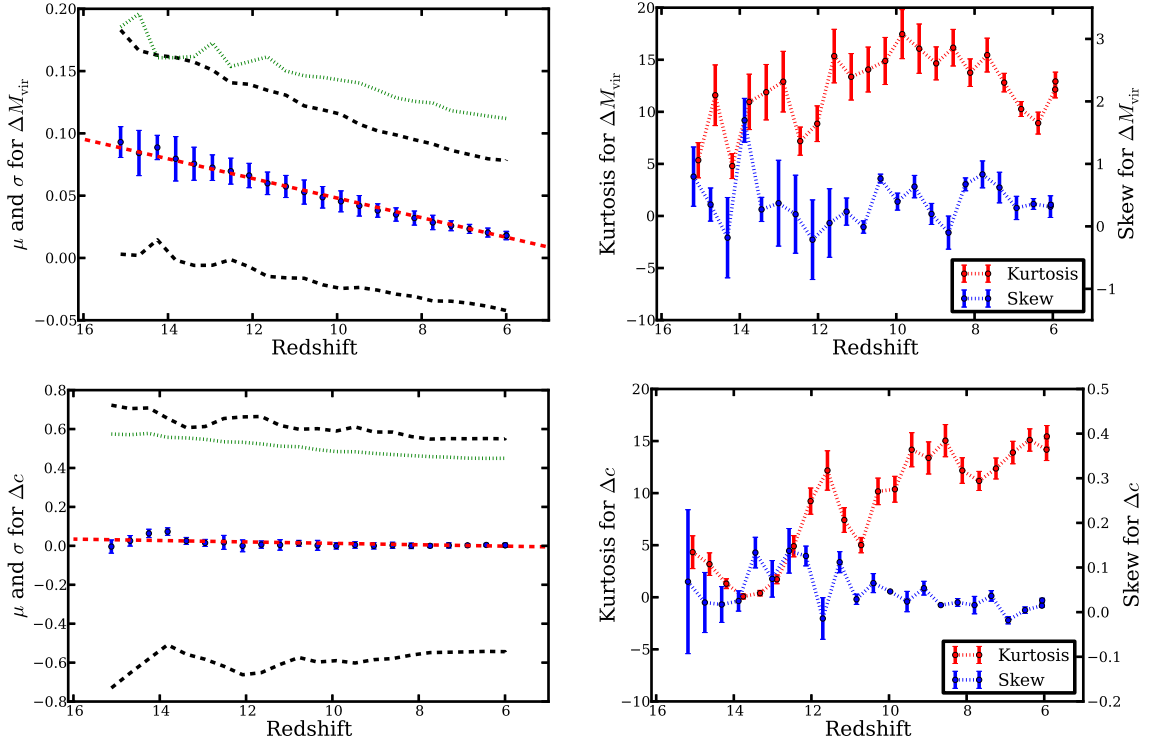


Figure III.3: Mean, standard deviation, and RMS (*left column*) and skew and excess kurtosis (*right column*) as functions of redshift for  $\Delta M_{\text{vir}}$  (*top row*) and  $\Delta c$  (*bottom row*). In the left column,  $\mu$  is plotted as blue points, and  $\mu \pm \sigma$  is plotted as the black dashed line, and RMS values are plotted as a green dotted line. The red dashed line is a linear fit to the mean. We find a significant trend for  $\mu$  for  $\Delta M_{\text{vir}}$  to be more positive at higher redshift and gradually shift toward zero as the simulation progresses, with a fit function of  $\mu_{\Delta M_{\text{vir}}} = (7.88 \pm 0.17) \times 10^{-3}z - (3.07 \pm 0.14) \times 10^{-2}$ . The mean for  $\Delta c$ , however, remains at or very near zero for most of the simulation and is fit by  $\mu_{\Delta c} = (3.62 \pm 0.95) \times 10^{-3}z - (2.34 \pm 0.84) \times 10^{-2}$ . The  $\Delta M_{\text{vir}}$  and  $\Delta c$  distributions narrow over time, with a slight decrease in  $\sigma$ . In the right column, we plot skew (blue line) and excess kurtosis (red line). Skew is positive for much of the simulation for  $\Delta M_{\text{vir}}$ , but is much smaller for  $\Delta c$ . Kurtosis is large (much more peaked than Gaussian) for both  $\Delta M_{\text{vir}}$  and  $\Delta c$  throughout much of the simulation, and especially at later redshift.



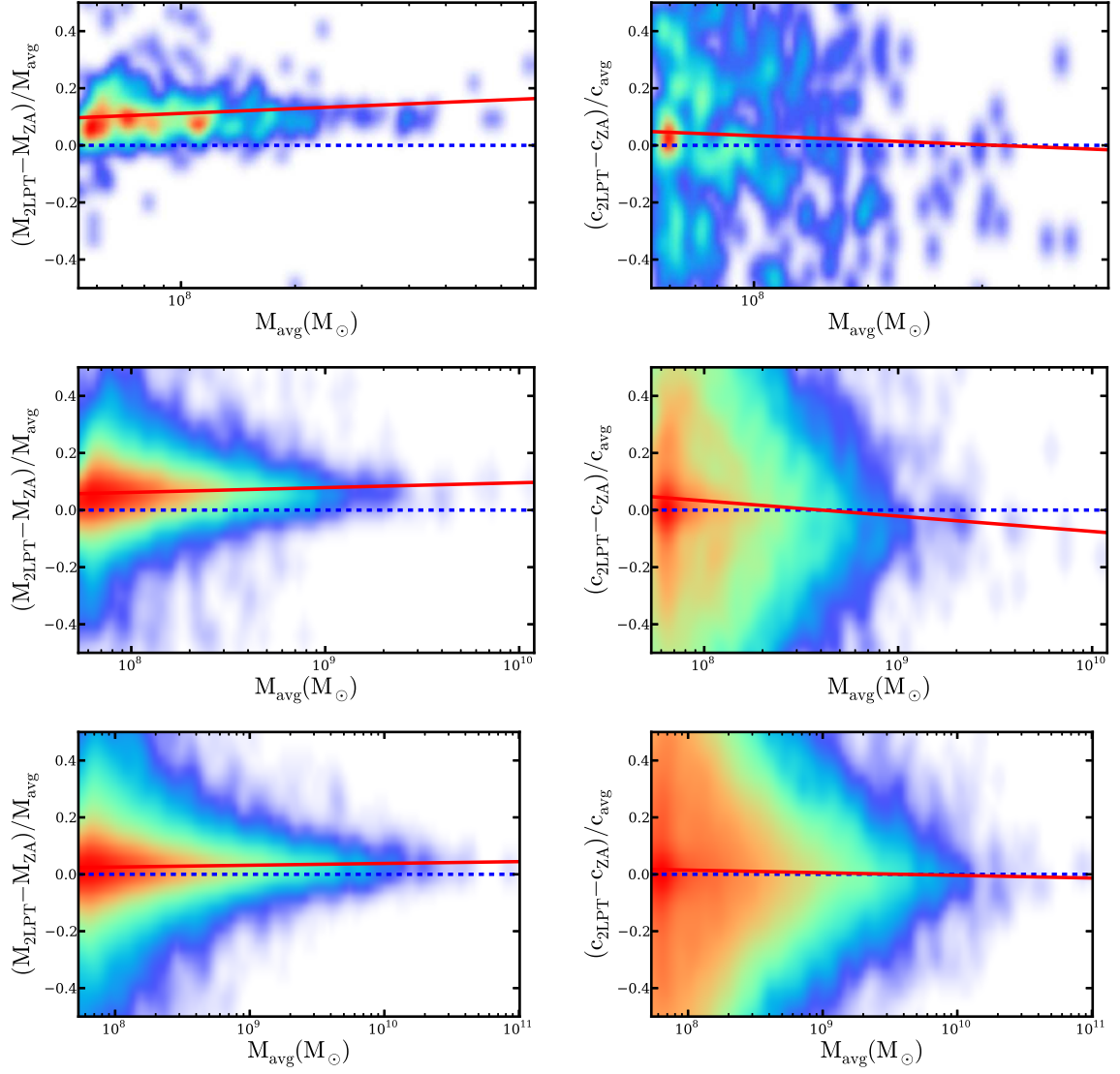


Figure III.4:  $\Delta M_{\text{vir}}$  (left column) and  $\Delta c$  (right column) as functions of  $M_{\text{vir,avg}}$ . Halos are counted in 2-D rectangular bins and smoothed with a Gaussian kernel with a logarithmic color scale. The red line is the least-squares best fit to the data. The blue dashed line at zero is provided to guide the eye. The three rows again correspond to snapshots at  $z = 14.7$ ,  $z = 10.3$ , and  $z = 6.0$ . We again see the overall offset for positive  $\Delta M_{\text{vir}}$  as before, and additionally find that more massive halo pairs are more likely to have even larger  $\Delta M_{\text{vir}}$ , especially at high redshift. Fit equations for the left column panels are  $\Delta M_{\text{vir}} = 5.6 \times 10^{-2} M_{\text{vir,avg}} - 0.33$ ,  $\Delta M_{\text{vir}} = 1.7 \times 10^{-2} M_{\text{vir,avg}} - 7.3 \times 10^{-2}$ , and  $\Delta M_{\text{vir}} = 6.4 \times 10^{-3} M_{\text{vir,avg}} - 2.5 \times 10^{-2}$ , respectively. Concentration show a small but opposite trend for more massive halos to be more concentrated in ZA than in 2LPT. The right column panels have fit equations  $\Delta c = -5.3 \times 10^{-2} M_{\text{vir,avg}} + 0.46$ ,  $\Delta c = -4.5 \times 10^{-2} M_{\text{vir,avg}} + 0.46$ , and  $\Delta c = -9.3 \times 10^{-3} M_{\text{vir,avg}} + 8.9 \times 10^{-2}$ , respectively.

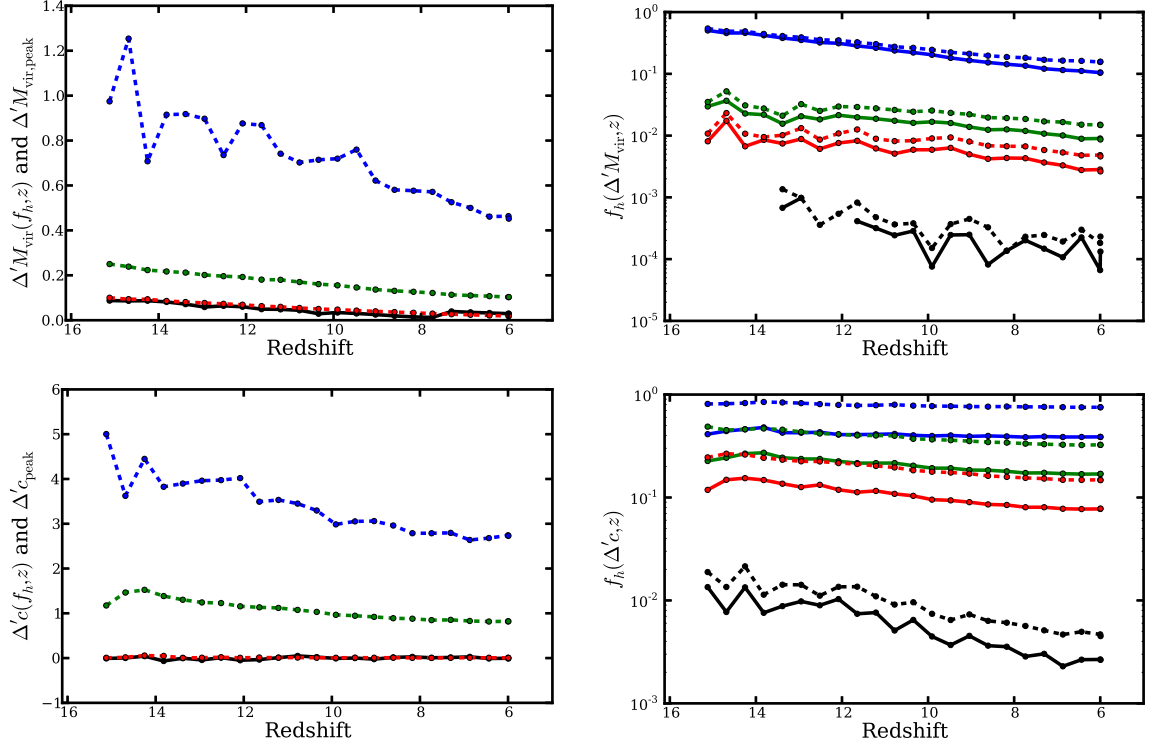


Figure III.5: Fractional error distributions statistics for  $\Delta'M_{\text{vir}}$  (top row) and  $\Delta'c$  (bottom row) as functions of redshift. *Left column:* The  $\Delta'q$  of the peak of the distribution (black line), and the  $\Delta'q$  where 50% (red dashed line), 10% (green dashed line), and 1% (blue dashed line) of the halos fall at or above  $\Delta'q$ . As with distributions of  $\Delta M_{\text{vir}}$ ,  $\Delta'M_{\text{vir}}$  has the largest positive displacement at high redshift and steadily decreases throughout the simulation. Additionally,  $\Delta'c$  maintains a peak near zero and has a spread much larger than that of  $\Delta'M_{\text{vir}}$ . *Right column:* The fraction of halos with  $\Delta'q$  greater than 0.10 (solid blue line), 0.50 (solid green line), 1.00 (solid red line), and 4.00 (solid black line). The dashed lines additionally count halo pairs with  $\Delta'q$  lower than the corresponding equivalent displacements of -0.09, -0.33, -0.50, and -0.80, respectively (see Equation III.22). We find that 50% of 2LPT halos are at least 10% more massive than their ZA companions at  $z = 15$ , reducing to 10% by  $z = 6$ . Halos in 2LPT are at least twice as concentrated for 12% of halos at  $z = 15$  and 7.8% of halos at  $z = 6$ .

## CHAPTER IV

### Supermassive Black Holes and Their Hosts

#### IV.1 Introduction

The study of the evolution of galaxies and the growth of the supermassive black holes at their cores go hand in hand. Although the typical length scales for the two can vary by many orders of magnitude, they seem inexorably linked. Observational correlations between galaxy and supermassive black hole properties hint at an underlying co-evolution driven by shared mechanisms.

##### IV.1.1 Galaxy Properties

How do we describe a galaxy? Being extended, resolvable objects, galaxies provide a unique wealth of observable characteristics not obtainable from point sources such as stars. While many characteristics can be deduced about point sources, the actual observations themselves come down to measuring position on the sky and measuring flux as a function of frequency and time. From this information, all that we know about stars and other point sources, such as temperature, age, size, and composition, can be inferred. However, for extended objects like galaxies, we are given more to work with.

###### IV.1.1.1 Color

A galaxy's color is determined by its stellar component. While a galaxy in itself may be resolvable, for all but the most nearby of galaxies, individual stars are not. What we see when looking at a particular small section of a galaxy is the averaged-together light from stars in that section.

Broadly, bluer late-type spirals have a  $u - r$  color of around  $1.3 - 2.0$ , while redder early-type galaxies have a  $u - r$  color of around  $2.3 - 2.7$ . The color of a galaxy can be a good indicator for its age and evolutionary stage. Star formation processes generally tend

to produce many smaller, cooler, redder stars and fewer larger, hotter, bluer stars. These small, cool stars are much longer-lived than their massive counterparts, while the large, warm stars are much brighter. After star formation turns off, the short-lived blue stars begin to die off, and the galaxy becomes redder, as more of the fraction of total light comes from the red end of the population.

#### **IV.1.1.2 Morphology**

The extended nature of galaxies allows us to observe their morphology. The classification scheme originally devised by Hubble (1926) places galaxies into the four broad categories: elliptical, spiral, lenticular, and irregular. Elliptical galaxies tend to be larger, redder, have less gas, and dominated by more radial orbits. Spiral galaxies tend to be smaller, bluer, have more gas, and have more of a disk component. Spirals can have a number of arms, a central bulge, and a central bar. Lenticular galaxies are middle-of-the-road galaxies, with both a strong central bulge like an elliptical, and an extended disk like a spiral, however without spiral arms. Irregular galaxies tend to defy this simple classification scheme, and can be found in any number of configurations.

Figure IV.1 is a cartoon of the classification scheme. To the left of the diagram are elliptical galaxies. The subcategories are an indication of the shape of the galaxy, with the most spherical on the left and progressing to more flattened shapes to the right. On the right of the diagram are spiral galaxies. These are broken into two branches, based on whether or not the galaxy contains a central bar. Moving from right to left, the spiral arms of the galaxies become more tightly wound, and the central bulges become more dominant. At the center of the diagram where the spiral fork meets the elliptical line, lie lenticular galaxies. Irregular galaxies are, as the name would imply, irregular and do not fall on the diagram.

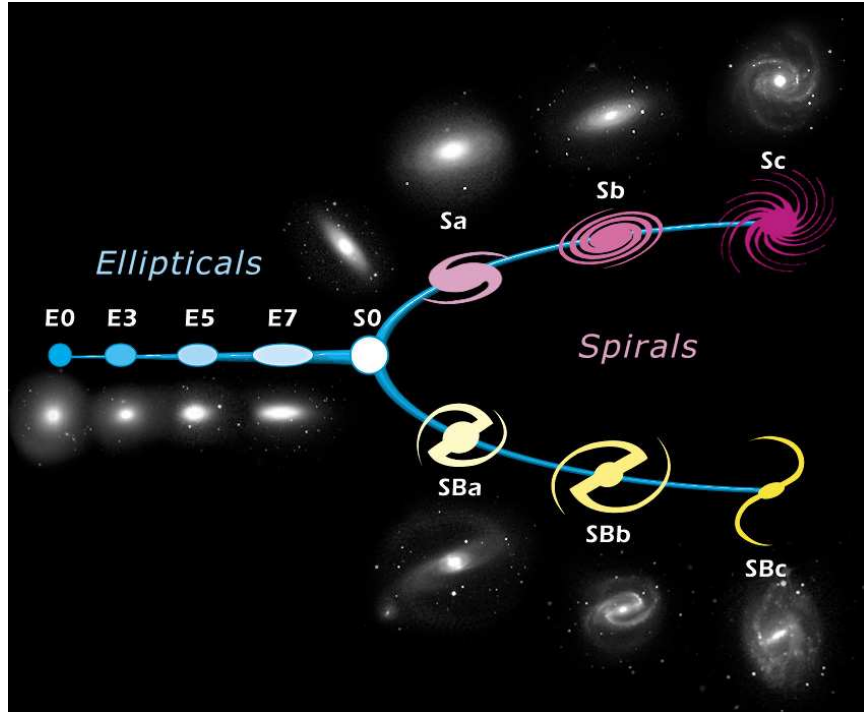


Figure IV.1: The Hubble tuning fork. On the left of the diagram are elliptical galaxies. E0 galaxies are the most spherical, while E7 are the most flattened or elongated. S0 are lenticular galaxies. The top branch on the right are spiral galaxies with no bar, while the bottom right branch are spiral galaxies with a bar. Both progress from tightly wound spiral arms and large bulges to loosely wound spiral arms and small to no bulges, going from Sa to Sc or SBa to SBc.

#### IV.1.2 Supermassive Black Hole Properties

A non-merging black hole, much like an elementary particle, can be described simply by its mass, charge, and spin. Its effect on its local spacetime, infalling matter, and surrounding environment all come back to these three parameters. However, determination of these parameters and the study of how black holes interact with their surroundings can be quite involved.

Black holes are, by their very nature, black, and difficult to observe. We cannot see light emitted directly from a black hole as we would a star, since a black hole is defined as an object massive and compact enough to not allow light within its event horizon to escape. We are forced, therefore, to employ other methods of measuring black holes.

Thus far, the majority of progress in the measurement of black hole properties has been in measuring mass. There are a number of ways to measure the mass of a black hole. Here, we will briefly discuss masers, stellar dynamics, gas dynamics, and reverberation mapping as methods of measuring a supermassive black hole's mass.

Astrophysical masers are sources of stimulated spectral line emission in the microwave band formed in regions of high-density gas comprised of molecules such as hydroxyl, formaldehyde, and water (Lo, 2005). Since the emission frequencies of these sources are very well constrained, high-accuracy Doppler shifts can be determined. These Doppler shifts can then be used to determine velocities for the masers, and thus how much mass is enclosed by their orbits. If these masers lie very close to the supermassive black hole (SMBH) in the center of their galaxy, the enclosed mass can be constrained to be primarily that of the SMBH.

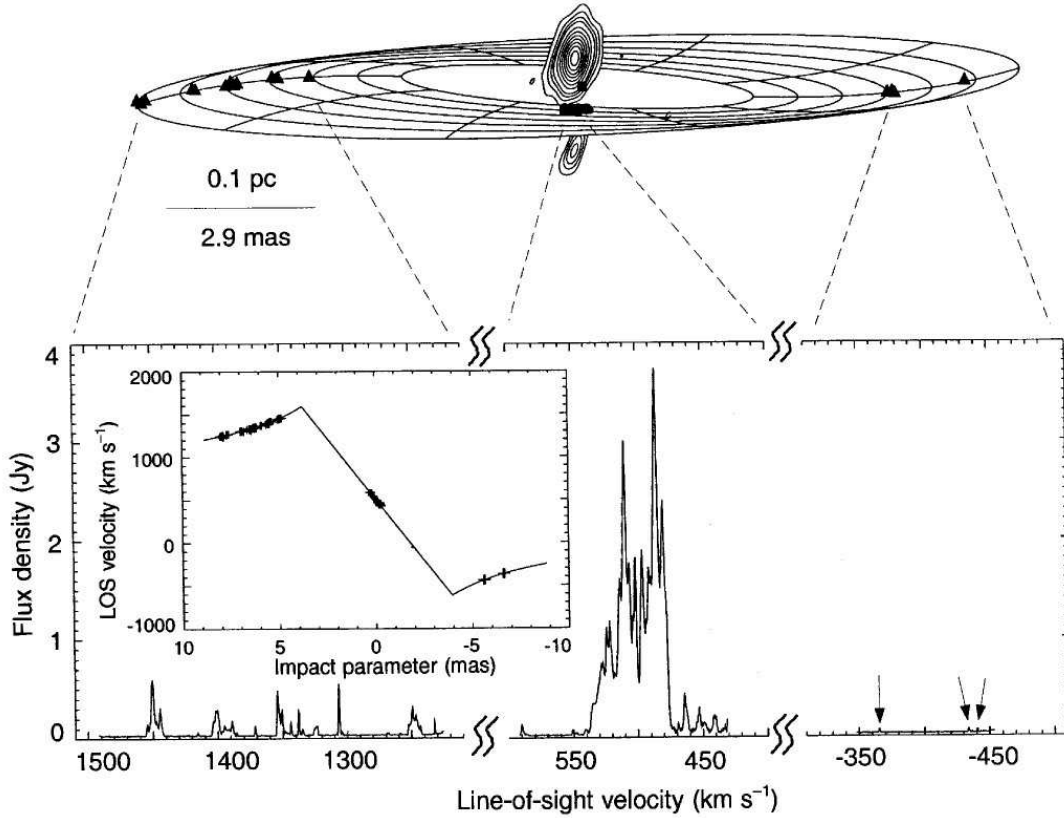


Figure IV.2: Maser orbits fit to a warped disk for NGC4258. Masers can also be useful for distance determinations. Here, the positions and velocities of water masers are able to be fit to a warped disk model surrounding a supermassive black hole. This allows the interpolation of physical radii away from the black hole, giving us both the black hole mass and an standard ruler to allow precise determination of the distance to NGC4258. (Herrnstein et al., 1999)

Stellar dynamics and gas dynamics both probe light coming from matter near the black hole. The width of broadened spectral lines from either the stars or gas can be used to determine a velocity dispersion for the matter local to the SMBH. This velocity dispersion, therefore, can then be used to determine the potential through which the matter is traveling, and thus the mass of the black hole.

A special case of stellar dynamics for which the orbits of the constituent stars can be resolved—namely, for the case of our own Milky Way—adds another dimension to our knowledge of the stellar orbits. Over time, we can observe the proper motion on the sky for these orbits. Combining these measurements with Doppler measurements for radial

velocity yields full orbital solutions. Then, it simply requires Kepler’s laws to determine the mass of the SMBH.

Reverberation mapping can be thought of as “echo-mapping” the gas disk around a SMBH. Continuum emission very near the black hole travels outward and stimulates broad line emission in surrounding gas. Any changes in the continuum emission will take time to propagate to the broad line region, since the speed of light is finite. By measuring the timing difference in the change in continuum emission and change in stimulated broad line emission, the physical distance from the SMBH to the broad line region can be inferred. With this radius, and the velocity of the gas in the broad line region measured by the width of the broadened lines, a black hole mass can be determined (Blandford & McKee, 1982).

### IV.1.3 Correlations

Correlations between varying properties of galaxies and black holes can provide much deeper insight into the dynamics that shape the evolution of both. Of particular interest here are the fundamental plane of elliptical galaxies, the  $M - \sigma$  relation, and the green valley-AGN relation.

#### IV.1.3.1 The M-Sigma Relation

If we consider the all the observable properties of a galaxy and compare them to the mass of its SMBH, the tightest correlation can be found with the velocity dispersion  $\sigma$  of the galaxy’s bulge. Such a tight correlation is surprising, as the sphere of influence of a typical SMBH does not extend much past order a few pc, while bulges exist on scales of a kpc or greater. In essence, the supermassive black hole and the outer edges of the bulge shouldn’t “feel” each other. Nevertheless, the correlation is indeed there, suggesting some mechanism that influences—or is influenced by—both of them. Gültekin et al. (2009) use a sample of 49  $M_{BH}$  measurements and 19 upper limits to measure this correlation, and find  $\log(M_{BH}/M_{\odot}) = \alpha + \beta \log(\sigma/200 \text{ km s}^{-1})$  with  $(\alpha, \beta, \epsilon_0) = (8.12 \pm 0.08 M_{\odot}, 4.24 \pm 0.41 M_{\odot}, 0.44 \pm 0.06 M_{\odot})$  for all galaxies and  $(\alpha, \beta, \epsilon_0) = (8.23 \pm 0.08 M_{\odot}, 3.96 \pm 0.42 M_{\odot}, 0.31 \pm$



$0.06M_{\odot})$  for ellipticals, where  $\epsilon_0$  is the intrinsic scatter in the relation.

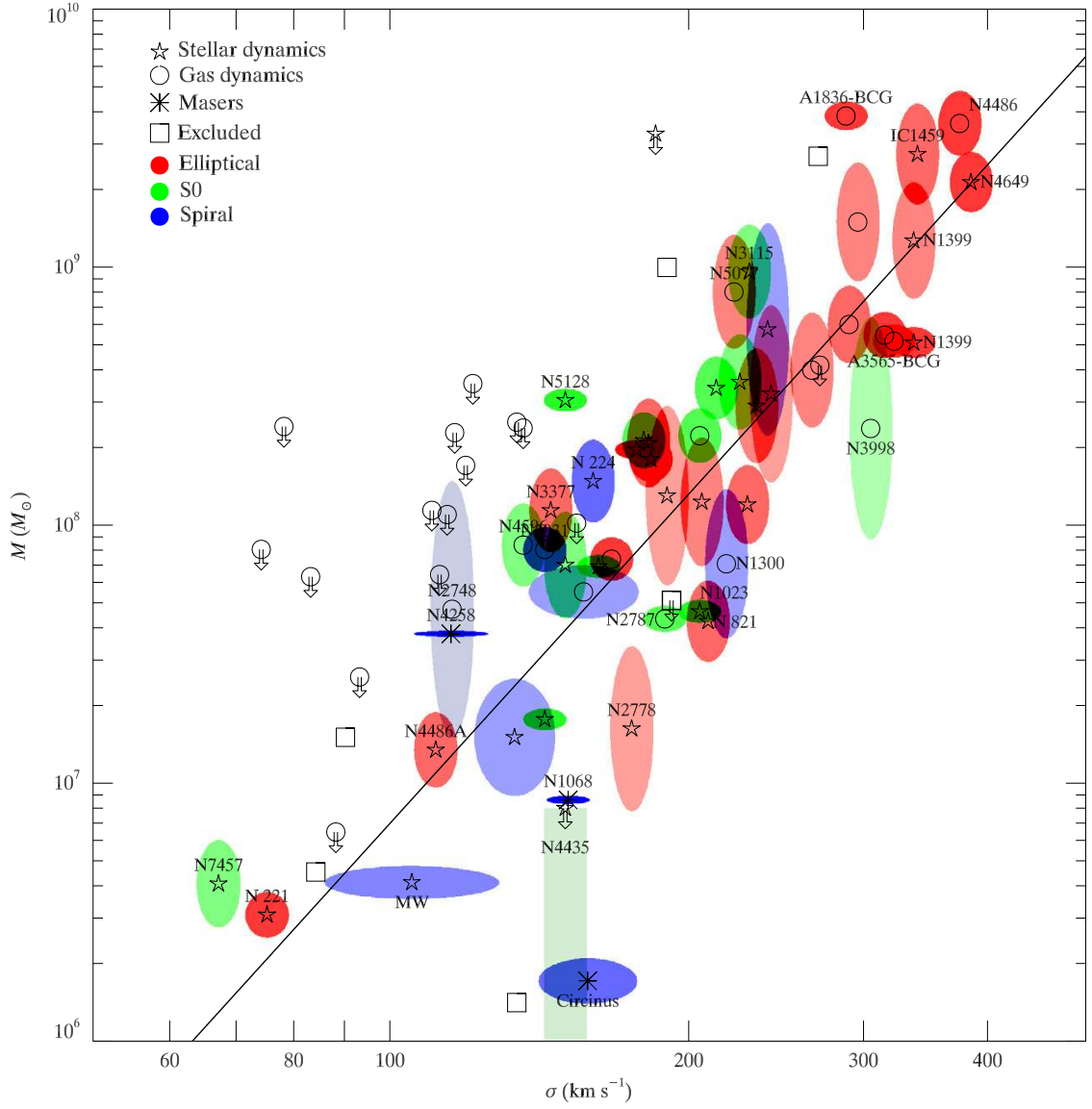


Figure IV.3: The  $M$ - $\sigma$  relation for galaxies with dynamical measurements. Black hole mass is plotted vs velocity dispersion of its host spheroid. The symbols represent the method by which the black hole mass was measured: pentagrams for stellar dynamics, circles for gas dynamics, and asterisks for masers. Upper limits are given by arrows. Error ellipses are colored by galaxy type, with red for ellipticals galaxies, green for lenticular galaxies, and blue for spiral galaxies. The saturation of the color is inversely proportional to the area of the ellipse. For this sample, the best fit relation is  $M_{BH} = 10^{8.12} M_{\odot} (\sigma/200 \text{ km s}^{-1})^{4.24}$ . Galaxies not included in this fit are labeled as squares. (Gültekin et al., 2009)

#### IV.1.3.2 The Fundamental Plane

While not a direct correlation with the properties of supermassive black holes, the fundamental plane of elliptical galaxies offers insight into the characteristics of their hosts. The fundamental plane is a three-parameter correlation between properties of elliptical galaxies: velocity dispersion, effective radius, and surface brightness. This correlation (Figure IV.4) between these three parameters is tighter than the combination of any two alone (Djorgovski & Davis, 1987). The fit for this correlation can be given as  $\log R_e = 0.36(\langle I \rangle_e / \mu_B) + 1.4 \log \sigma_0$ , where  $R_e$  is the effective radius in kpc,  $\langle I \rangle_e$  is the mean surface brightness interior to  $R_e$  in units of  $\mu_B$ , and  $\sigma_0$  is the velocity dispersion in  $\text{km s}^{-1}$  (Binney & Merrifield, 1998).

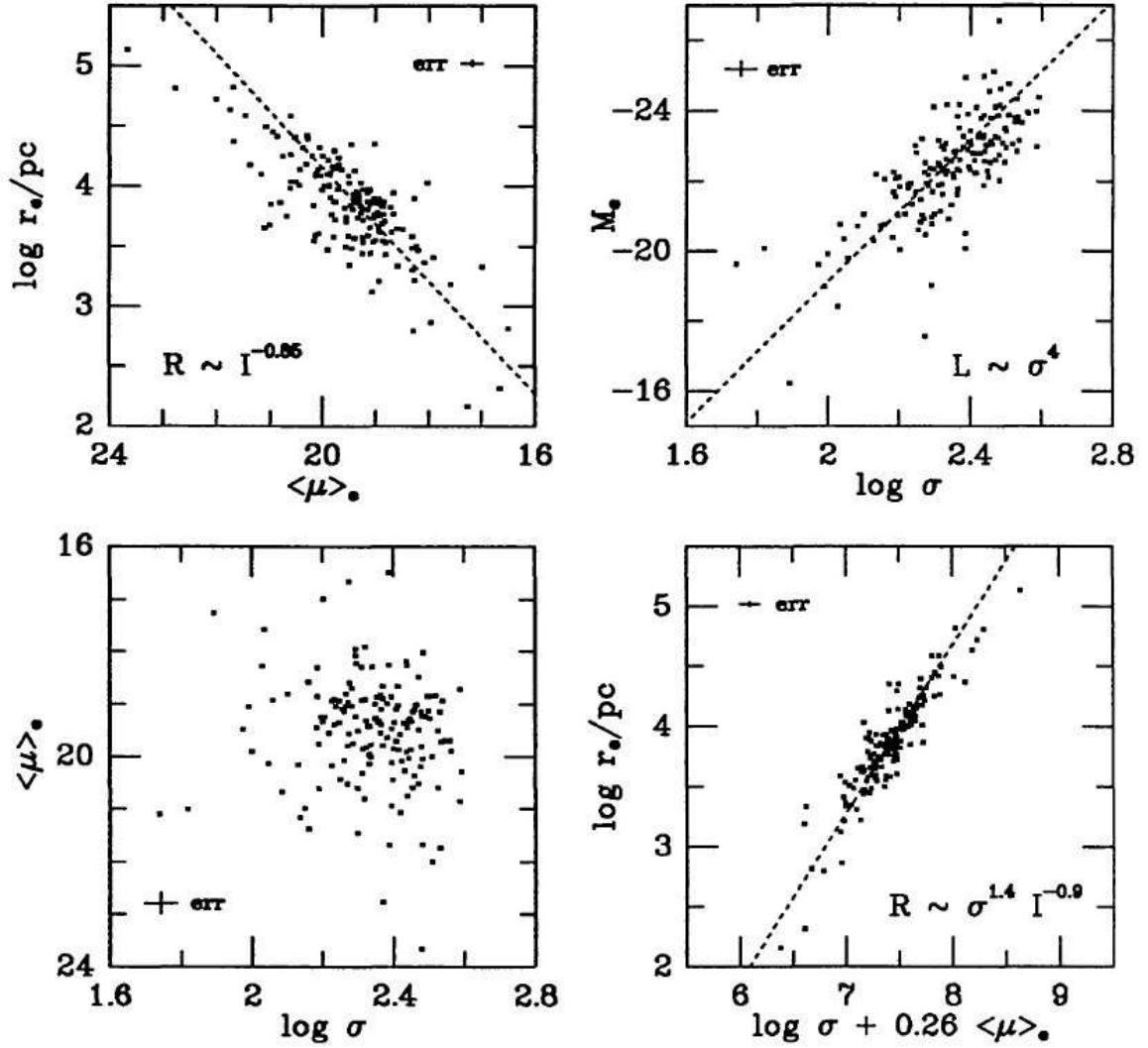


Figure IV.4: The fundamental plane for elliptical galaxies. *Top panels:* The top panels show the one-parameter scaling relations, with the relation between radius and mean surface brightness on the left and the relation between luminosity and velocity dispersion (the Faber-Jackson relation) on the right. *Bottom left:* The relation between the surface brightness and velocity dispersion. This is an almost face-on view of the fundamental plane. *Bottom right:* The relation between the effective radius and the combination of surface brightness and velocity dispersion. This is the edge-on view of the fundamental plane. (Kormendy & Djorgovski, 1989)

### IV.1.3.3 The Green Valley

When considering both the color and stellar mass of a galaxies, a correlation emerges where many galaxies lie in either the “blue cloud” of bluer, lower mass galaxies, or the “red

sequence” of redder, generally higher mass galaxies. The area between these two is known as the “green valley” and, while not as populated as the blue cloud or red sequence, holds special interest when active galactic nuclei (AGN) are considered. AGN are very luminous regions at the centers of some galaxies. Schawinski et al. (2010) show that galaxies falling on the green valley are much more likely to host AGN than galaxies on the blue cloud or red sequence, hinting at an underlying link between the evolution of galaxies, and the activity at their centers.

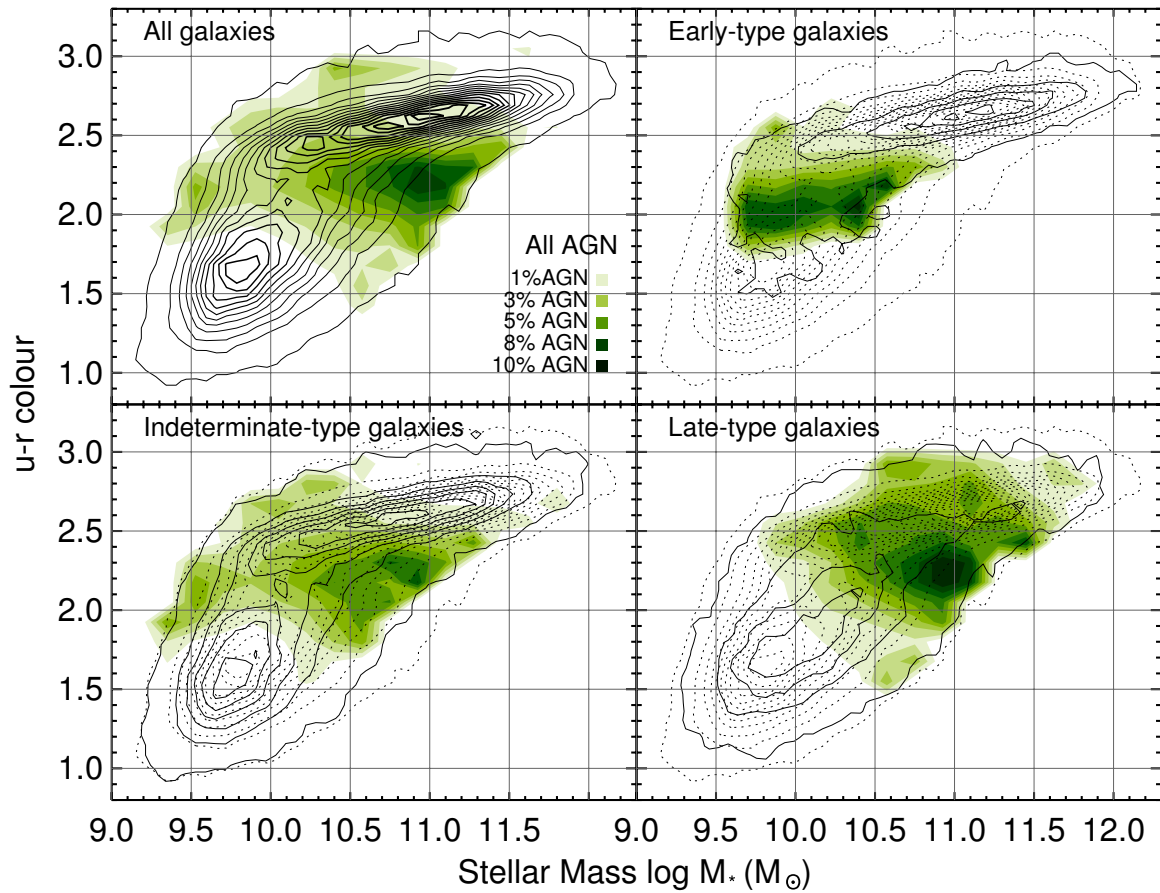


Figure IV.5: Distribution of the fraction of galaxies containing AGN. Galaxy color in  $u-r$  is plotted vs stellar mass. The contours are the galaxy population for all galaxies (top-left), early-type galaxies (top right), intermediate-type galaxies (bottom left), and late type galaxies (bottom right). For the three sub-samples, dotted contours represent the full sample for comparison. The green shaded contours represent the fraction of galaxies in that subsample that contain active galactic nuclei. It can be clearly seen that the AGN fraction is highest for galaxies falling within the green valley. (Schawinski et al., 2010)

## IV.2 Galaxy Evolution

### IV.2.1 Dark Matter Halos

Every galaxy resides inside a dark matter halo. Often about an order of magnitude larger in both radius and mass than the baryonic component, dark matter halos dominate the large-scale behavior of galaxies. Dark matter is matter that is thought to interact very weakly or not at all with light and ordinary matter, except gravitationally. Evidence for dark matter comes from a number of sources, including the relatively flat rotational velocity curve of galaxies, the velocity dispersion of galaxies, gravitational lensing measurements, galaxy clustering, and the offset between the gas and dominant mass measured in the Bullet cluster. Here we will briefly discuss the evidence from flat rotation curves.

If there were no dark matter component and only the baryonic components (i.e. stars and gas) contributed to the galactic potential, we would expect the rotational velocity of galaxies to fall off with radius. However, observations show that the rotation curve remains relatively flat (Rubin et al., 1980). Figure IV.6 shows several observed rotation curves.

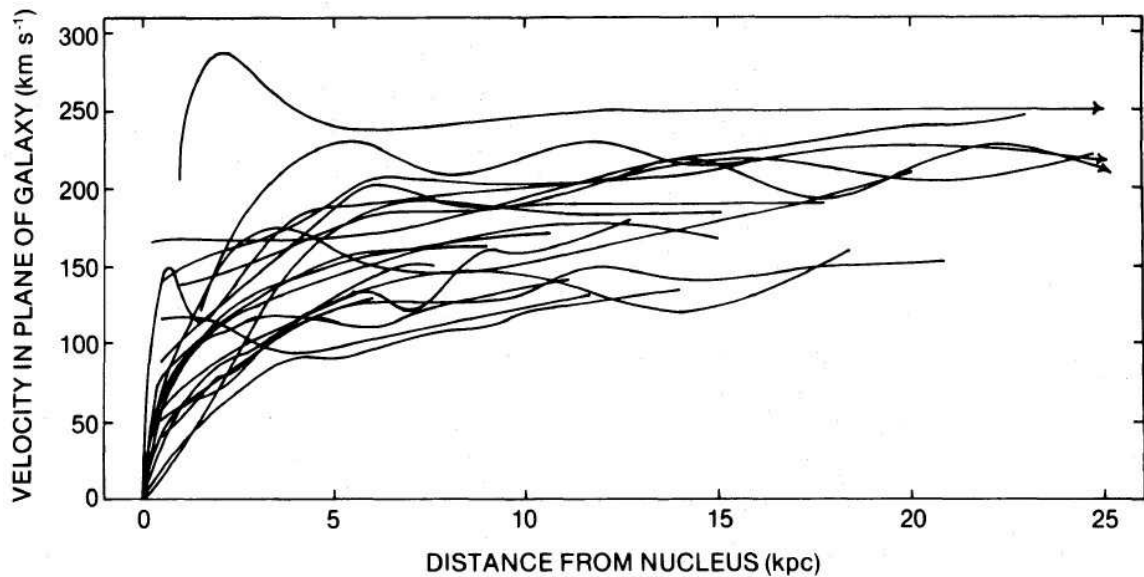


Figure IV.6: Rotation curves for 21 Sc galaxies. It is readily identifiable that the rotation curves do not fall off as would be expected for galaxies without a dark matter component. (Rubin et al., 1980)

Navarro et al. (1997b) found that dark matter halos generally follow the same density

profile, regardless of mass. This universal dark matter density profile can be given as

$$\rho(r) \propto \frac{1}{(r/a)(1+r/a)^2}, \quad (\text{IV.1})$$

where  $a$  is the radius where the profile transitions from an  $r^{-1}$  power law to an  $r^{-3}$  power law.

### IV.2.2 Galaxy Mergers

Galaxy mergers are the fundamental mechanism by which galaxies grow and evolve. Collisions between galaxies trigger processes that can alter nearly all the properties of the galaxies. Naturally, mergers increase the mass of galaxies. Starting from small perturbations in the early universe, gravity slowly pulls matter together to form larger and larger clumps. These clumps of gas and dark matter eventually form stars, beginning what we think of as typical galaxies, and over time, these galaxies merge together into larger and larger galaxies.

Mergers affect many other properties of galaxies as well. Mergers distort the shapes of galaxies, causing long tidal tails to form and the entire morphology to appear irregular. The disk structures of spiral galaxies that form from the settling of the rotational component are distorted and “puffed up” into components with ever increasing bulge-like properties.

Mergers can trigger wide-scale starburst events, where a large portion of gas goes into the formation of stars. Much of the gas component of the galaxy can subsequently be blown out by the winds from the supernovae of short-lived O and B stars. This shuts off star formation, and as the stellar population is no longer replenished with new high-mass stars, the galaxy becomes progressively redder as large stars die.

The general trend is for mergers to move galaxies from the right side of the Hubble tuning fork towards the left, turning blue, gas rich spirals into red, gas poor ellipticals. This process is aided by the AGN feedback also triggered during galaxy mergers, as we discuss in the following section.

### IV.3 Supermassive Black Hole Growth

Supermassive black holes grow by two primary mechanisms, binary mergers and gas accretion. Through a combination of these, black holes can grow to as large as  $\sim 10^9\text{--}10^{10} M_\odot$  by  $z = 0$ .

#### IV.3.1 Binary Mergers

When two galaxies merge, the supermassive black holes at their hearts begin a process that will eventually lead to their coalescence. There are generally thought to be three stages to this journey. First, the black holes sink towards the center of the merged galaxy through mass segregation and dynamical friction until they form a bound orbit with each other. Then, the black holes tighten their orbit through three-body scattering of nearby stars. Finally, as the black holes become close enough together for general relativistic effects to come into play, gravitational waves are emitted and radiate away the remaining orbital energy until the binary coalesces.

##### IV.3.1.1 Dynamical Friction and Inspiral

During the majority of the inspiral process, the black holes do not “feel” each other’s gravitational pull. Instead, interactions with the galaxy itself push the holes together.

As it travels through a galaxy, a black hole—or any massive body—is slowed by the surrounding field of matter. Gravitational attraction pulls surrounding matter toward the black hole. However, as the black hole is moving with respect to the local medium, the attracted particles will tend to fall behind the black hole. This creates a wake of overdensity that gravitationally attracts the black hole from behind and slows its velocity. Chandrasekhar (1943) develops this notion of dynamical friction for the motion of a star through a sea of other stars. If the distribution of velocities of the surrounding particles is Maxwellian, the acceleration on the black hole can be written as

$$\frac{d\mathbf{v}_M}{dt} = -\frac{4\pi G^2 M \rho \ln \Lambda}{v_M^3} \left[ \text{erf}(X) - \frac{2X}{\sqrt{\pi}} e^{-X^2} \right] \mathbf{v}_M, \quad (\text{IV.2})$$

where  $v_M$  is the velocity of the black hole,  $M$  is its mass,  $\rho$  is the density of surrounding matter,  $\text{erf}$  is the error function,  $\ln \Lambda$  is the Coulomb logarithm, and  $X \equiv v_M/(\sqrt{2}\sigma)$  where  $\sigma$  is the velocity dispersion of the surrounding medium (Binney & Tremaine, 1988). As the black hole is slowed by dynamical friction, it loses angular momentum and sinks towards the center of the galaxy's potential well.

#### **IV.3.1.2 The Final Parsec Problem**

Dynamical friction and mass segregation can only take us so far. Once the black holes are close enough together, they form a bound binary orbit. This generally occurs for separations of around a few to tens of parsecs. This presents a problem, however, since the orbit needs to shrink to around  $10^{-2}$ – $10^{-3}$  pc in order for gravitational wave emission to remove energy from the orbit in a significant amount. The orbit can be tightened with three-body scattering of stars that wander through the orbit of the binary, however, in the spherical galaxies where mergers often take place, there is a depletion of stars with orbits that intersect the binary. Khan et al. (2011), however, show that the non-spherical, triaxial potential typical of post-merger galaxy remnants can efficiently funnel stars through the orbit of the black hole binary with sufficient intensity to tighten the binary orbit to the gravitational wave regime.

#### **IV.3.1.3 Gravitational Waves and Recoil Kicks**

Once the black hole binary separation reaches the point where strong field general relativistic effects come into play, we no longer require external influences to nudge the black holes together. In the final plunge toward coalescence, the black hole binary sheds energy through emission of gravitational radiation. As energy is radiated away, the binary tightens its orbit until the two black holes merge into one. Following this coalescence, the resultant black hole undergoes a “ringdown” phase, in which the distorted space time settles back down into a black hole that can again be simply described by mass, charge, and spin.

The emission of gravitational waves has two interesting consequences. First, the radiation from two merging supermassive black holes is extremely loud, and can potentially



provide an observational signature of the process for gravitational wave observatories. Second, the gravitational waves carry linear momentum, leading to a recoil “kick” imparted to the black hole merger remnant.

Recent advances in numerical relativity simulations have provided a much deeper insight into the black hole binary merger process than has been previously available. Waveforms produced from these simulations (Figure IV.7) can be used to predict what gravitational wave observatories such as LIGO and LISA would expect to observe for signals originating from merging supermassive black hole binaries. Having these waveforms as templates for comparison to data can greatly increase the signal to noise ratio for these detectors, potentially allowing the gravitational wave events to be seen among the sea of noise. These waveforms produced from simulations of the last few orbits of inspiral through the merger and ringdown can be combined with waveforms suggested from post-Newtonian approximations for the longer duration inspiral to provide a complete extended signal to match against.

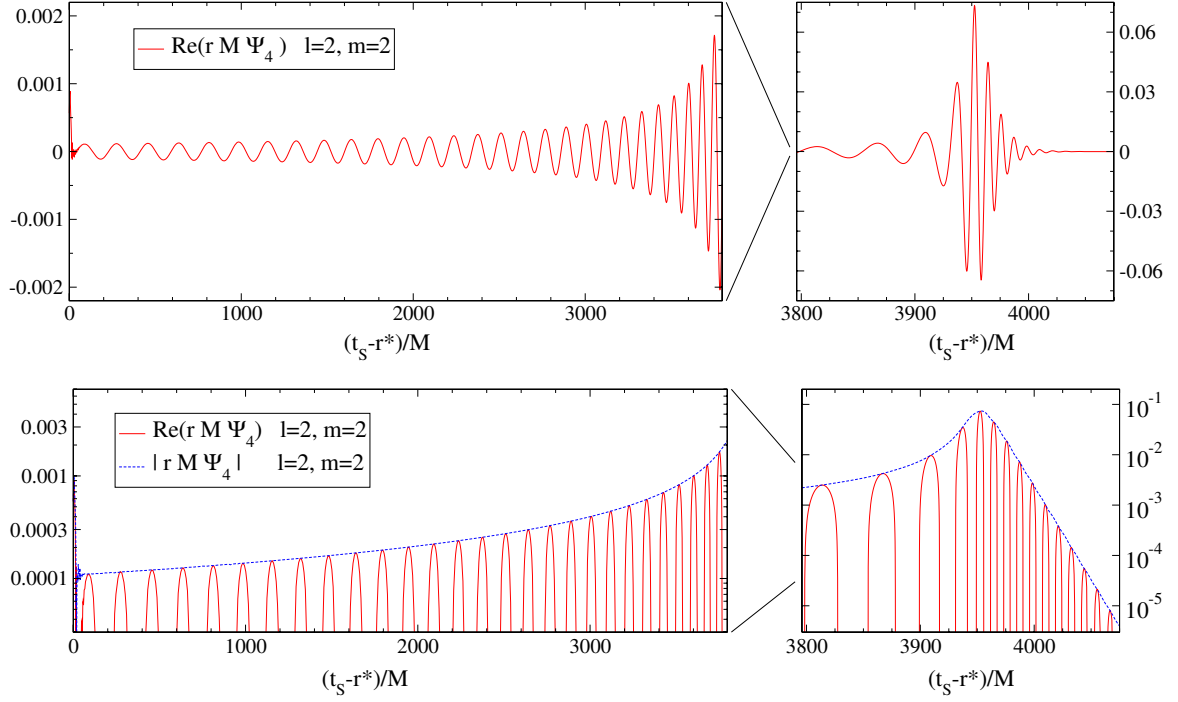


Figure IV.7: Gravitational waveform for an equal-mass, non-spinning black hole binary merger. This is the final waveform, extrapolated to infinity, from the numerical relativity simulation of Scheel et al. (2009). The waveform is shown on the top panel with a linear y-axis and on the bottom panel with a logarithmic y-axis. The left panels are the earlier stages of inspiral, and the right panels show the merger and ringdown stages.

For asymmetric mergers, gravitational radiation is emitted anisotropically. This causes a recoil kick, in which the gravitational waves impart a net velocity to the final black hole with respect to the original center of mass. The magnitude and direction of this kick are dependent on the mass ratio of the binary and the spins of the two black holes—in all, a 7-dimensional parameter space. This large parameter space has been largely explored with numerical relativistic simulations, and analytic equations can be fit to the data to predict the recoil from a given merger configuration. Holley-Bockelmann et al. (2008), give these equations as

$$\mathbf{v}_{kick} = (1 + e) \left[ \hat{\mathbf{x}}(v_m + v_{\perp} \cos \xi) + \hat{\mathbf{y}}v_{\perp} \sin \xi + \hat{\mathbf{z}}v_{\parallel} \right], \quad (\text{IV.3})$$

where

$$v_m = A \frac{q^2(1-q)}{(1+q)^5} \left[ 1 + B \frac{q}{(1+q)^2} \right], \quad (\text{IV.4})$$

$$v_\perp = H \frac{q^2}{(1+q)^5} \left( \alpha_2^\parallel - q \alpha_1^\parallel \right), \quad (\text{IV.5})$$

$$v_\parallel = K \cos(\Theta - \Theta_0) \frac{q^2}{(1+q)^5} \left( \alpha_2^\perp - q \alpha_1^\perp \right). \quad (\text{IV.6})$$

Here, the fitting constants are  $A = 1.2 \times 10^4 \text{ km s}^{-1}$ ,  $B = -0.93$ ,  $H = (7.3 \pm 0.3) \times 10^3 \text{ km s}^{-1}$ , and  $K = (6.0 \pm 0.1) \times 10^4 \text{ km s}^{-1}$ . The  $\hat{z}$  unit vector is in the direction of the orbital angular momentum, and  $\perp$  and  $\parallel$  refer to components perpendicular and parallel to  $\hat{z}$ , respectively. The fitting parameters are the eccentricity  $e$ , the mass ratio  $q \equiv M_2/M_1$ , and the reduced spin parameters  $\alpha_i \equiv S_i/M_i^2$  where  $S$  is the spin angular momentum. The orientation of the merger is given by the angles  $\Theta$ ,  $\Theta_0$ , and  $\xi$  (Holley-Bockelmann et al., 2008).

Slices through this parameter space are shown in Figure IV.8. For certain configurations of the merger, the recoil velocity can be very high. Very asymmetric mergers can produce recoils as high as  $\sim 4000 \text{ km s}^{-1}$ . These large recoils can be enough for the black hole to escape the potential well of its host galaxy and be ejected. Even less extreme recoil kicks can affect the evolution of black holes, as the kicked black hole can oscillate about its host's center, potentially changing its local gas environment and accretion rate.

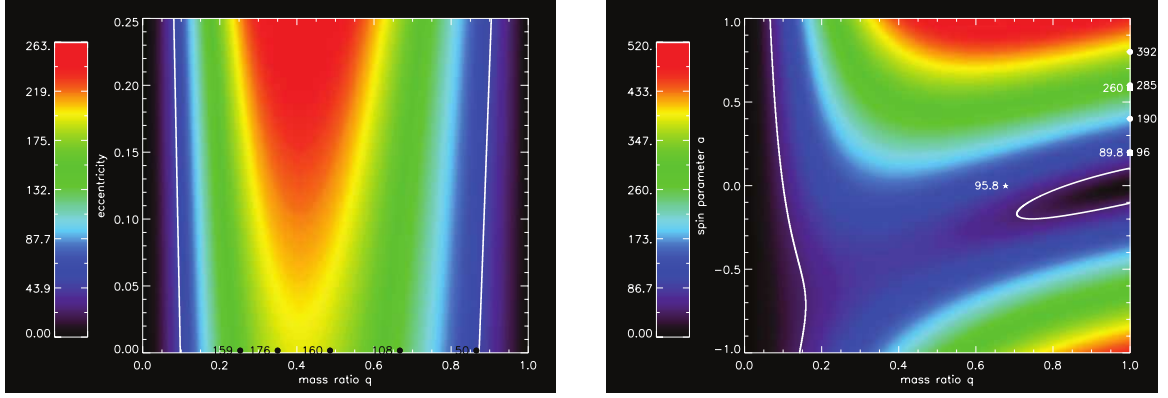


Figure IV.8: *Left:* Gravitational wave recoil velocity from a merger of nonspinning black holes as a function of eccentricity and mass ratio. Data from numerical relativity simulations (González et al., 2007) are overlaid along the zero eccentricity line. The overlaid white contours are the escape velocity of a typical globular cluster,  $50 \text{ km s}^{-1}$ . *Right:* Gravitational wave recoil kick velocity as a function of spin parameter and mass ratio for a merger of spinning black holes on a circular orbit with spins perpendicular to the orbital plane of the binary and anti-aligned with each other. Again, the  $50 \text{ km s}^{-1}$  escape velocity of a globular cluster is overlaid as white contours. Results from numerical relativity simulations are over-plotted: squares for Koppitz et al. (2007), circles for Herrmann et al. (2007), and star for Brüggmann et al. (2004). (Holley-Bockelmann et al., 2008)

### IV.3.2 Accretion

Although mergers play an important role in the evolution of supermassive black holes, gas accretion can often dominate in terms of mass growth. Gas can fall into a black hole in a number of ways. Here, we will discuss accretion onto a moving black hole, spherical accretion onto a stationary black hole, and disk accretion onto a stationary black hole.

#### IV.3.2.1 Bondi-Hoyle-Lyttleton Accretion

Let us first consider a massive object, in this case our black hole, moving through a uniform density gas medium. Just as in the case of dynamical friction, particles close enough to the black hole will feel a gravitational attraction, causing them to move toward the black hole. As they move closer, the black hole is also moving through the medium, causing the gas particles to focus behind the black hole. As the particle stream reaches the wake directly

behind the black hole, it collides with opposing streams, causing the angular momentum to go to zero. If these particles are bound, they will proceed to fall onto the black hole. Hoyle & Lyttleton (1939) derive an impact parameter for which particles will be accreted,

$$\sigma < \sigma_{HL} = \frac{2GM}{v_\infty^2}, \quad (\text{IV.7})$$

and a mass accretion from the wake column at a rate of

$$\dot{M}_{HL} = \pi \sigma_{HL}^2 v_\infty \rho_\infty = \frac{4\pi G^2 M^2 \rho_\infty}{v_\infty^3}, \quad (\text{IV.8})$$

where  $v_\infty$  and  $\rho_\infty$  are the velocity and density far away from the black hole, respectively. Expanding upon this analysis, Bondi & Hoyle (1944) suggest that the accretion rate should rather be

$$\dot{M}_{BH} = \frac{2\alpha \pi G^2 M^2 \rho_\infty}{v_\infty^3}, \quad (\text{IV.9})$$

where  $\alpha$  is a constant between 1 and 2, with a typical value of around 1.25.

For an accretor at rest in an isotropic gas medium, one would expect accretion to be a spherical process. Bondi (1952) considers this configuration, and finds the accretion rate for this “temperature-limited” case to be

$$\dot{M}_{Bondi} = \frac{2\pi G^2 M^2 \rho_\infty}{c_{s,\infty}^3}, \quad (\text{IV.10})$$

where  $c_{s,\infty}$  is the speed of sound far away from the black hole.

Extrapolating between this result and the “velocity-limited” case of Equation IV.9 suggests (Bondi, 1952)

$$\dot{M}_{BH} = \frac{2\pi G^2 M^2 \rho_\infty}{(c_{s,\infty}^2 + v_\infty^2)^{3/2}} \quad (\text{IV.11})$$

as an order of magnitude estimate of the more general case of accretion. Numerical simulations (Shima et al., 1985) suggest an additional factor of 2 is needed for better agreement

with simulation results, giving us a generally applicable formula for the accretion rate,

$$\dot{M}_{BH} = \frac{4\pi G^2 M^2 \rho_\infty}{(c_{s,\infty}^2 + v_\infty^2)^{3/2}}. \quad (\text{IV.12})$$

#### IV.3.2.2 Disk Accretion and Active Galactic Nuclei

Active galactic nuclei play a fundamental role in the evolution of both supermassive black holes and their host galaxies. As gas falls in to a black hole in the center of a galaxy, its angular momentum forces it into an accretion disk. As matter moves towards the SMBH, it transfers its gravitational potential energy to thermal energy. For accretion disks around supermassive black holes, this can cause the disk to emit large amounts of electromagnetic radiation (Lin & Papaloizou, 1996).

This emitted radiation is important in a number of ways. Most critical to the SMBH itself is the radiation pressure exerted on infalling matter. This radiation pressure sets an upper limit on the rate of accretion, as there is a point where the force from emitted radiation balances the force of gravity for infalling gas (Rybicki & Lightman, 1979). This limit, known as the Eddington limit, is given by

$$L_{Edd} = 4\pi G M c m_H / \sigma_T = 1.25 \times 10^{38} \text{erg s}^{-1} (M/M_\odot), \quad (\text{IV.13})$$

where  $c$  is the speed of light,  $m_H$  is the mass of hydrogen, and  $\sigma_T$  is the Thompson cross section.

The radiation given off by the accretion disk affects galactic properties as well. Powerful AGN can strip away gas from the center of the galaxy, halting star formation. This can quickly change a galaxy from a blue, gaseous, star forming galaxy into one that is red, dry, and dead.

## IV.4 Conclusion

We have seen that galaxies and the supermassive black holes at their centers both have their most dramatic periods of evolution around the same time. Galaxy mergers grow both the galaxy and the SMBH. Galaxies grow and become more elliptical as mergers bring in additional mass on orbits that can disrupt their gaseous disks. These mergers also bring in counterpart supermassive black holes that fall toward the center of the galaxy and merge with the central SMBH, while also triggering accretion events and AGN feedback that pump energy back into the galaxy, shutting off star formation.

### IV.4.1 Correlations

In light of these shared growth mechanisms, the correlations mentioned in Section IV.1 begin to move from a purely observational coincidence to a natural result of co-evolution. The  $M-\sigma$  relation is a natural byproduct of the simultaneous growth of supermassive black holes and their galaxies during merger events. The mass of the SMBH increases due to the merging of binary companions and increased levels of accretion, while the host mass, and thus velocity dispersion, increases due to the infalling galaxy itself. Likewise, the overabundance of AGN in galaxies lying in the green valley is the consequence of simultaneous change. Mergers both trigger highly luminous AGN feedback and cause an inexorable shift from the blue cloud, through the green valley, to the red sequence. Even the increase in scatter of the  $M-\sigma$  relation at low masses can be explained by the galaxies having lower mass, and therefore being more likely to allow a gravitational wave recoil kicked black hole of a given velocity to escape.

### IV.4.2 Open Questions

In the end, there remain a number of open questions. How can very large supermassive black holes form so early? What is dark matter actually made of? How do galaxies retain their black holes if merger recoils can kick them with velocities greater than the escape velocity of the galaxy? Over what range are our correlations truly valid? These are just

some of the questions that are currently being investigated, and promise to provide a rich field of study for years to come.



## **CHAPTER V**

### **Conclusion**

## BIBLIOGRAPHY

- Abel, T., Bryan, G. L., & Norman, M. L. 2000, *Astrophys. J.*, 540, 39
- . 2002, *Science*, 295, 93
- Alvarez, M. A., Bromm, V., & Shapiro, P. R. 2006, *Astrophys. J.*, 639, 621
- Alvarez, M. A., Wise, J. H., & Abel, T. 2009, *Astrophys. J., Lett.*, 701, L133
- Barkana, R., & Loeb, A. 2001, *Phys. Rep.*, 349, 125
- Behroozi, P. S., Wechsler, R. H., & Wu, H.-Y. 2013, *Astrophys. J.*, 762, 109
- Binney, J., & Merrifield, M. 1998, *Galactic Astronomy*, Princeton Series in Astrophysics (Princeton University Press)
- Binney, J., & Tremaine, S. 1988, *Galactic Dynamics*, Princeton Series in Astrophysics (Princeton University Press)
- Blandford, R. D., & McKee, C. F. 1982, *Astrophys. J.*, 255, 419
- Bondi, H. 1952, *Mon. Not. R. Astron. Soc.*, 112, 195
- Bondi, H., & Hoyle, F. 1944, *Mon. Not. R. Astron. Soc.*, 104, 273
- Bouchet, F. R., Colombi, S., Hivon, E., & Juszkievicz, R. 1995, *Astron. Astrophys.*, 296, 575
- Bouwens, R. J., Illingworth, G. D., Oesch, P. A., et al. 2012, *Astrophys. J., Lett.*, 752, L5
- Brügmann, B., Tichy, W., & Jansen, N. 2004, *Phys. Rev. Lett.*, 92, 211101
- Bryan, G. L., & Norman, M. L. 1998, *Astrophys. J.*, 495, 80
- Buchert, T. 1994, *Mon. Not. R. Astron. Soc.*, 267, 811
- Buchert, T., Melott, A. L., & Weiss, A. G. 1994, *Astron. Astrophys.*, 288, 349
- Bullock, J. S., Kolatt, T. S., Sigad, Y., et al. 2001, *Mon. Not. R. Astron. Soc.*, 321, 559
- Bykov, A. M., Paerels, F. B. S., & Petrosian, V. 2008, *Space Sci. Rev.*, 134, 141
- Chandrasekhar, S. 1943, *Astrophys. J.*, 97, 255
- Couchman, H. M. P., & Rees, M. J. 1986, *Mon. Not. R. Astron. Soc.*, 221, 53
- Crocce, M., Pueblas, S., & Scoccimarro, R. 2006, *Mon. Not. R. Astron. Soc.*, 373, 369
- Davis, M., Efstathiou, G., Frenk, C. S., & White, S. D. M. 1985, *Astrophys. J.*, 292, 371

- Djorgovski, S., & Davis, M. 1987, *Astrophys. J.*, 313, 59
- Efstathiou, G., Davis, M., White, S. D. M., & Frenk, C. S. 1985, *Astrophys. J., Suppl. Ser.*, 57, 241
- Einasto, J., Klypin, A. A., Saar, E., & Shandarin, S. F. 1984, *Mon. Not. R. Astron. Soc.*, 206, 529
- Eke, V. R., Navarro, J. F., & Steinmetz, M. 2001, *Astrophys. J.*, 554, 114
- Fan, X., Narayanan, V. K., Lupton, R. H., et al. 2001, *Astron. J.*, 122, 2833
- Gao, L., Navarro, J. F., Cole, S., et al. 2008, *Mon. Not. R. Astron. Soc.*, 387, 536
- Gnedin, N. Y., & Ostriker, J. P. 1997, *Astrophys. J.*, 486, 581
- González, J. A., Sperhake, U., Brüggmann, B., Hannam, M., & Husa, S. 2007, *Phys. Rev. Lett.*, 98, 091101
- Gültekin, K., Richstone, D. O., Gebhardt, K., et al. 2009, *The Astrophysical Journal*, 698, 198
- Heger, A., Fryer, C. L., Woosley, S. E., Langer, N., & Hartmann, D. H. 2003, *Astrophys. J.*, 591, 288
- Heger, A., & Woosley, S. E. 2002, *Astrophys. J.*, 567, 532
- Heitmann, K., Lukić, Z., Habib, S., & Ricker, P. M. 2006, *Astrophys. J., Lett.*, 642, L85
- Herrmann, F., Hinder, I., Shoemaker, D., Laguna, P., & Matzner, R. A. 2007, *Astrophys. J.*, 661, 430
- Herrnstein, J. R., Moran, J. M., Greenhill, L. J., et al. 1999, *Nature*, 400, 539
- Holley-Bockelmann, K., Gültekin, K., Shoemaker, D., & Yunes, N. 2008, *Astrophys. J.*, 686, 829
- Holley-Bockelmann, K., Wise, J. H., & Sinha, M. 2012, *Astrophys. J., Lett.*, 761, L8
- Hoyle, F., & Lyttleton, R. A. 1939, *Proceedings of the Cambridge Philosophical Society*, 35, 405
- Hubble, E. P. 1926, *Astrophys. J.*, 64, 321
- Islam, R. R., Taylor, J. E., & Silk, J. 2003, *Mon. Not. R. Astron. Soc.*, 340, 647
- Jenkins, A. 2010, *Mon. Not. R. Astron. Soc.*, 403, 1859
- Jeon, M., Pawlik, A. H., Greif, T. H., et al. 2012, *Astrophys. J.*, 754, 34
- Khan, F. M., Just, A., & Merritt, D. 2011, *Astrophys. J.*, 732, 89

- Klypin, A. A., & Shandarin, S. F. 1983, *Mon. Not. R. Astron. Soc.*, 204, 891
- Klypin, A. A., Trujillo-Gomez, S., & Primack, J. 2011, *Astrophys. J.*, 740, 102
- Komatsu, E., Dunkley, J., Nolte, M. R., et al. 2009, *Astrophys. J., Suppl. Ser.*, 180, 330
- Koppitz, M., Pollney, D., Reisswig, C., et al. 2007, *Phys. Rev. Lett.*, 99, 041102
- Kormendy, J., & Djorgovski, S. 1989, *Ann. Rev. Astron. Astrophys.*, 27, 235
- Kuhlen, M., & Faucher-Giguère, C.-A. 2012, *Mon. Not. R. Astron. Soc.*, 423, 862
- Lin, D., & Papaloizou, J. 1996, *Annual Review of Astronomy and Astrophysics*, 34, 703
- Lo, K. Y. 2005, *Ann. Rev. Astron. Astrophys.*, 43, 625
- Lukić, Z., Heitmann, K., Habib, S., Bashinsky, S., & Ricker, P. M. 2007, *Astrophys. J.*, 671, 1160
- Macciò, A. V., Dutton, A. A., & van den Bosch, F. C. 2008, *Mon. Not. R. Astron. Soc.*, 391, 1940
- Madau, P., Haardt, F., & Rees, M. J. 1999, *Astrophys. J.*, 514, 648
- Madau, P., & Rees, M. J. 2001, *Astrophys. J., Lett.*, 551, L27
- Muñoz-Cuartas, J. C., Macciò, A. V., Gottlöber, S., & Dutton, A. A. 2011, *Mon. Not. R. Astron. Soc.*, 411, 584
- Nadarajah, S. 2005, *Journal of Applied Statistics*, 32, 685
- Navarro, J. F., Frenk, C. S., & White, S. D. M. 1996, *Astrophys. J.*, 462, 563
- . 1997a, *Astrophys. J.*, 490, 493
- . 1997b, *Astrophys. J.*, 490, 493
- Neto, A. F., Gao, L., Bett, P., et al. 2007, *Mon. Not. R. Astron. Soc.*, 381, 1450
- Prada, F., Klypin, A. A., Cuesta, A. J., Betancort-Rijo, J. E., & Primack, J. 2012, *Mon. Not. R. Astron. Soc.*, 423, 3018
- Press, W. H., & Schechter, P. 1974, *Astrophys. J.*, 187, 425
- Reed, D. S., Bower, R., Frenk, C. S., Jenkins, A., & Theuns, T. 2007, *Mon. Not. R. Astron. Soc.*, 374, 2
- Rubin, V. C., Ford, W. K. J., & Thonnard, N. 1980, *Astrophys. J.*, 238, 471
- Rybicki, G. B., & Lightman, A. P. 1979, *Radiative processes in astrophysics* / George B. Rybicki, Alan P. Lightman (Wiley, New York :), xv, 382 p. :

- Schawinski, K., Urry, C. M., Virani, S., et al. 2010, *The Astrophysical Journal*, 711, 284
- Scheel, M. A., Boyle, M., Chu, T., et al. 2009, *Phys. Rev. D*, 79, 024003
- Scoccimarro, R. 1998, *Mon. Not. R. Astron. Soc.*, 299, 1097
- Shapiro, P. R., & Giroux, M. L. 1987, *Astrophys. J., Lett.*, 321, L107
- Shima, E., Matsuda, T., Takeda, H., & Sawada, K. 1985, *Mon. Not. R. Astron. Soc.*, 217, 367
- Sinha, M., & Holley-Bockelmann, K. 2009, *Mon. Not. R. Astron. Soc.*, 397, 190
- . 2010, *Mon. Not. R. Astron. Soc.*, 405, L31
- Sirko, E. 2005, *Astrophys. J.*, 634, 728
- Springel, V. 2005, *Mon. Not. R. Astron. Soc.*, 364, 1105
- Springel, V., Yoshida, N., & White, S. D. M. 2001, *New Astron*, 6, 79
- Tanaka, T., Perna, R., & Haiman, Z. 2012, *Mon. Not. R. Astron. Soc.*, 425, 2974
- Tegmark, M., Silk, J., Rees, M. J., et al. 1997, *Astrophys. J.*, 474, 1
- Venkatesan, A., Tumlinson, J., & Shull, J. M. 2003, *Astrophys. J.*, 584, 621
- Voit, G. M. 2005, *Reviews of Modern Physics*, 77, 207
- Wechsler, R. H., Bullock, J. S., Primack, J. R., Kravtsov, A. V., & Dekel, A. 2002, *Astrophys. J.*, 568, 52
- White, M. 2001, *Astron. Astrophys.*, 367, 27
- Zel'dovich, Y. B. 1970, *Astron. Astrophys.*, 5, 84
- Zhao, D. H., Jing, Y. P., Mo, H. J., & Börner, G. 2009, *Astrophys. J.*, 707, 354
- Zhao, D. H., Mo, H. J., Jing, Y. P., & Börner, G. 2003, *Mon. Not. R. Astron. Soc.*, 339, 12